

¹ Masters Thesis: The Evolution of Fault Slip
² Surfaces with Cumulative Displacement

³ Kelian Dascher-Cousineau

⁴ May 18, 2017

⁵ **Abstract**

⁶ Fault slip surface roughness determines fault strength, friction and dy-
⁷ namic fault processes. Wear models and field observations suggest that
⁸ roughness decreases with cumulative displacement. However, measurements
⁹ have yet to isolate the effect of displacement from other possible controls,
¹⁰ such as lithology or tectonic setting. We present an unprecedentedly large
¹¹ fault surface dataset collected in and around the San-Rafael Desert, S.E.
¹² Utah, United States. In the study area, faults accommodated regional ex-
¹³ tension at shallow 1 to 3 *km* depth and are hosted in the massive, well
¹⁴ sorted, high porosity Navajo and Entrada sandstones. Existing detailed
¹⁵ stratigraphic throw profile provide a maximum constraint for displacement.
¹⁶ Where cross-sectional exposure is good, we measure exact displacement im-
¹⁷ parted on slip surfaces using offset in marker horizons. Thereby, we isolate
¹⁸ for the effect of displacement during the embryonic stages of faulting (0
¹⁹ to 60 *m* in displacement). Our field observations indicate a clear compo-
²⁰ sitional and morphological progression from isolated joints or deformation

bands towards smooth, continuous and mirror-like fault slip surfaces with increasing displacement. To quantify these observations, slip surfaces were scanned with a white light interferometer, a laser scanner and a ground based Lidar. Together these instruments resolve more than eight decades of spatial bandwidth (from less than μm 's to m 's in scale). In so doing, to the best of our knowledge, we increase the existing data on published fault topographies by XXX fold (available HERE). Results indicate that roughness as defined by the power (P) at a given wavelength (λ) decreases with displacement (D) according to a power law, $P(\lambda) \propto D^{0.6 \pm 0.1}$. Trends are however subject to significant scatter. Roughness measurement associated with only maximum constraints on displacements corroborate this result—for a given displacement, minimum roughness is bounded by the later smoothing trend. In addition, we find that the maximum roughness is fixed—bounded a by a primordial roughness corresponding to that of joints surfaces and deformation band edges. Building upon our results, we propose a wear model to explain the evolution of faults with displacement. The basis of the model is supported by numerical simulations of crack initiation and growth using boundary element models Fri2D and growth by work-minimization (GROW). Our modelling provides the first insight into fault slip surface process consistent with observational constraints, i.e. fractal geometry and a nearly power-law decay with displacement, by using calling upon scale dependent strength, strength heterogeneity and scale invariant asperity failure by truncation.

⁴⁴ **Contribution of Authors**

⁴⁵ **1 Introduction**

⁴⁶ **1.1 Context**

⁴⁷ Faults are a characteristic feature of the Earth's brittle crust. Crustal permeability, seismicity, and mineralization are just few systems upon which faults act as
⁴⁸ major controls [?, ?]. In spite of their importance, some aspects of faults and their
⁴⁹ underlying processes remain poorly understood. What are the frictional properties
⁵⁰ of faults? How strong is a fault? How do faults mature as they evolve from small
⁵¹ to large displacement structures? Key factors such as pore pressure [?, ?], mineral
⁵² composition [?, ?, ?] and fault architecture [?, ?] have been shown to have impor-
⁵³ tant roles in the behavior of faults. However, these factors often fail to explain
⁵⁴ the highly heterogeneous, chaotic and hierarchical behaviour of faults. Complex
⁵⁵ fault geometry has long been proposed as a key factor in the faulting process.
⁵⁶ However, a detailed and robust exploration of the implications thereof has only re-
⁵⁷ cently garnered increasing attention. This change of pace mainly owes to advances
⁵⁸ in mathematical theory behind complex natural systems [?, ?], rapid advances
⁵⁹ computational abilities enabling more complex source models, technological ad-
⁶⁰ vances in high resolution surveying tools (GPS, photogrammetry and Lidar) and
⁶¹ detailed field studies of fault architecture [?, ?]. Fault geometry has since been in-
⁶² cluded as a key component of wholistic explanations for the mechanical behavior
⁶³ and evolution of faults (e.g. [?, ?, ?]).

⁶⁵ Fault zones generally comprise of a damage zone and fault core. The damage
⁶⁶ zone represents the halo of subsidiary fault features including smaller fault, frac-

67 tures, cleavage and veins. The fault core generally represents the zone in which
68 most of the displacement has taken place and is associated with intense comminu-
69 tions of the protolith [?, ?, ?]. Actual Slip on a fault occurs on discrete slip surfaces
70 within the fault core [?, ?, ?, ?]. These surfaces are not planar; they are rough [?].
71 Slickenlines, corrugations, mullions and jogs are all fault slip surface features which
72 reflect the multiscale nature of fault roughness [?, ?]. Field studies have found com-
73 mon characteristics in the statistical properties which describe the topography of
74 fault surfaces. These can be summarized as follows: 1) Fault surfaces topogra-
75 phies appear to be well defined by large fractal domains [?] , wherein 2) faults are
76 smoother at larger length scales [?, ?] and 3) are rougher in the slip-perpendicular
77 direction than in the slip-parallel direction [?, ?].

78 Fault roughness has been demonstrated to be critical in determining fault prop-
79 erties and corresponding scaling relationships. A series of field investigations,
80 laboratory experiments, analytical predictions and numerical simulation have ex-
81 plored the heterogeneous stresses and deformation patterns around complex fault
82 geometries around single fault steps, ramps and jogs (e.g. [?, ?, ?, ?, ?]), on simple
83 theoretical fault geometries (e.g. [?, ?]), and real or synthetic faults with geometri-
84 cally fractal bandwidths in two dimensions (e.g. [?, ?, ?, ?] and three dimensions
85 (e.g. [?, ?, ?, ?, ?])). Direct repercussion of complex stress patterns include the fol-
86 lowing: increased geometrical shear resistance [?]; increased and spatially variable
87 off-fault damage and fracture energy [?, ?, ?]; reduced stress drop [?] and impeded
88 slip budget [?]. In numerical simulations, zielke2017fault reports a nearly two-fold
89 decrease in earthquake moment release for a fault with realistic roughness com-
90 pared to its planar counterpart. Laboratory experiments comparing smooth and
91 rough surfaces show that with increasing roughness, friction increases [?], rate and

92 state $a - b$ slip stability increases [?], critical slip distance increases and rupture
93 nucleation dimension increases with surface roughness [?]. These features do ap-
94 pear in earthquake statistics. For example, bolstered by numerical simulations of
95 complex stress fields, Parsons, 2008, found that persistent clusters and gaps in
96 seismicity can be attributed to geometrical complexities on faults.

97 It is therefore increasingly evident that roughness is both a fingerprint of the
98 fundamental features of- and an active agent in the faulting process [?, ?, ?]. In
99 accordance, incorporating more complex sources geometries has become a more
100 frequent practice in forward and inverse dynamic earthquake rupture modelling
101 (e.g. [?, ?, ?]).

102 The measured magnitude of roughness is highly variable from one fault to
103 the other. While there has been significant progress in understanding the active
104 role of roughness in the faulting process, it remains unclear what determines the
105 complexity of fault geometry (e.g. [?, ?]). Sagy et al. (2007) noted a systematic de-
106 crease in roughness of ‘mature’, large displacement faults compared to ‘immature’
107 faults with low displacements. Similar results have been observed along reacti-
108 vated joints, in laboratory experiments [?], and in compilations of fault roughness
109 analysis [?, ?]. However, these data show only weak correlations between fault
110 roughness and cumulative displacement [?, ?]. These results are also put in ques-
111 tion by later experiments showing roughening with shear with normal loads higher
112 than 7.5 MPa [?]. Detailed qualitative field investigation have further shown that
113 slip geometry arises from net process between smoothing (i.e. asperity failure and
114 wear) and re-roughening (e.g. off-fault damage) [?].

115 If fault geometry changes as a fault accumulates displacement, it would have
116 a profound effect on fault mechanics and, correspondingly, seismology. However,

relating fault roughness to cumulative displacement is not trivial. Experiments cannot perform tests with realistic roughness over large enough displacement. It is also unclear how laboratory experiments scale up to natural faults because of the fractal scaling exhibited by natural fault systems. Exhumed fault slip surfaces are rarely well preserved. In the field, obtaining well-constrained displacement estimates is contingent on the presence of precise and accurate kinematic indicators (e.g. piercing points). Additionally, combining observations over a broad range of displacements is challenging. Consequently, it is unclear whether trends observed in compilations of roughness measurements from multiple faults are directly attributable to displacement or a combination other geological factors [?]. For instance, while comparing fault surfaces from geologically diverse datasets, variations in lithology, faulting regimes, temperature and depth may all be introducing further systematic variations.

The existence of a distinction between mature and immature faults and the precise characterization of this transition has far-reaching implications. As discussed above, earthquake sources parameters are sensitive to fault roughness. Correspondingly, an evolution of roughness with displacement implies that "not all fault should be treated equally". This prediction is consistent with more efficient energy radiation measured on mature faults compared to immature faults [?]; and changes in b-values associated with fault off-set [?]. Additionally, the evolution of roughness would have a corresponding effect on the architecture of a fault zone. The geometry of the fault surface modulates the architecture of the whole fault zone [?, ?, ?]. Changes in roughness require interaction between the slip surfaces and its direct surrounding (fault core), resulting in the formation of fault rock [?] and off-fault damage [?, ?]. The co-evolution evolution of the fault slip surface and

¹⁴² the fault zone as a whole is a novel insight the maturity of fault from a structural
¹⁴³ point of view.

¹⁴⁴ 1.2 Fault Roughness

¹⁴⁵ The deviation of fault surfaces from planarity formally defines roughness [?]. Pi-
¹⁴⁶ oneering studies used contact profilometers to measure the roughness of fracture
¹⁴⁷ and fault surfaces along discrete profiles [?, ?, ?, ?, ?]. Combined with the sur-
¹⁴⁸ face profile of the San Andreas fault, faults were found to exhibit fractal scaling
¹⁴⁹ over a remarkably broad range of length scales ranging over 10 orders of magni-
¹⁵⁰ tude—from 10^{-5} to $10^5 m$ [?, ?, ?]. Over these length scales, fractal scaling is said
¹⁵¹ to be statistically self-affine [?, ?].

¹⁵² A statistically self-affine profile along x with heights $h(x)$, is invariant under
¹⁵³ the affine transformation:

$$\begin{cases} x \rightarrow \lambda x \\ h \rightarrow \mu h \end{cases} \quad (1)$$

¹⁵⁴ This relation therefore implies an exponential relation between the scaling, λ
¹⁵⁵ (along x), and μ (along h) such that:

$$\mu = \lambda^\varsigma \quad (2)$$

¹⁵⁶ Where ς is a constant named the Hurst exponent [?].

¹⁵⁷ Many analytical methods exist to quantify the fractal roughness of faults [?, ?,
¹⁵⁸ ?]. Possibly most intuitive of these methods is the Root Mean Squared (*RMS*) as
¹⁵⁹ a function of scale. It is effectively a measure of topographic variance. For a given

₁₆₀ profile of length L with a point spacing of Δx with deviation h from the best fit
₁₆₁ line, the RMS is defined as follows:

$$RMS(L) = \sqrt{\frac{\Delta x}{L} \sum_{i=1}^{L/\Delta x} h_i^2} \quad (3)$$

₁₆₂ The RMS roughness of a fault or fracture exhibits a positive power-law scaling
₁₆₃ with segment length. A self-affine profile should therefore plot as a straight line
₁₆₄ on a log-log plot of the RMS as a function of the segment length with a slope
₁₆₅ equivalent to the Hurst exponent [?]. An alternative approach to describe the
₁₆₆ fractal roughness of faults has instead been the power spectrum and variations
₁₆₇ thereof (i.e. amplitude spectrum and power spectral density). By testing various
₁₆₈ fractal analytical tools on synthetic profiles [?] and surfaces [?], the power spectral
₁₆₉ analysis was shown to yield estimated of scaling exponent most robust to system
₁₇₀ size and Hurst exponent values. For a set of discretely sampled points, the power
₁₇₁ spectrum of a profile is the result of a Fourier transform. In practice it is obtained
₁₇₂ using a Fast Fourier Transform algorithm (FFT). The power spectrum describes
₁₇₃ a two dimensional surface profile as linear superposition of sinusoidal profiles dis-
₁₇₄ cretized over a fixed frequency domain. In the frequency domain, rougher profiles
₁₇₅ will have correspondingly higher amplitudes, or power. The power spectrum of a
₁₇₆ self-affine profile defines a power-law:

$$P(k) = Ck^{(-1-2\zeta)} \quad (4)$$

₁₇₇ Where $P(k)$ is the power at a given spatial frequency, k , C is the pre-factor and
₁₇₈ ζ is the Hurst exponent [?, ?, ?, ?].

₁₇₉ Early studies suggested that fault surfaces were approximately self-similar.

180 Self-similarity represents a self-affinity with a Hurst exponent is 1 [?]. The de-
181 velopments in laser scanner technology over the past decade, particularly terres-
182 trial laser scanners, enabled the detailed characterization of slip surfaces in three
183 dimension [?, ?, ?, ?, ?, ?, ?, ?, ?]. Later studies averaging cross-sectional profiles
184 through a fault surface suggested that smaller Hurst exponen less than 1 may bet-
185 ter characterize fracture surfaces and faults (e.g. [?, ?, ?, ?, ?]). Studies of natural
186 mode I crack surfaces have observed radially symetric, or isotropic, self-affinity
187 with a Hurst exponent of ~ 0.8 at all scales of observation ([?, ?]-and references
188 therein). Shear, or mode II cracks (i.e. faults) were found to differ in that they are
189 anisotropic. The Hurst exponent parallel to shear (~ 0.6) is smaller than that in
190 the shear-perpendicular direction (~ 0.8) [?, ?, ?, ?]. Overall, observations also show
191 that fault surfaces have distinctly smoother profiles along slip direction than per-
192 pendicular to slip [?, ?, ?]. The magnitude of the roughness, specified by the pref-
193 actor, C , in both directions is, however, subject to a substantial spread in values
194 over many orders of magnitude [?, ?]. Recent studies also report a minimum length
195 scale of grooving, a length scale at which slip surface is no longer anisotropic [?, ?].
196 This transitions typically occurs around 4 to 500 μm and roughly corresponds to
197 where the fractal scaling in the slip parallel and slip perpendicular direction meet.

198 Why are slip surfaces fractal? The fractal character of slip surfaces can be
199 explained by a range of processes. There is, however, no clear consensus in the ex-
200 isting literature. Candidate explanations include the superposition of random wear
201 processes processes, random fracture tip growth, and more ... Perhaps most topical
202 is the proposition of scale dependent strength as proposed by brodsky2016scale.
203 Using the aspect ratios of geometrical asperities as a measure of rock strength at
204 a given scale, they argued that fractal character of fault surfaces directly reflects

205 a scale dependence in rock strength. Moreover, a break in fractal scaling at the
206 $\approx XXX\mu m$ length scale is interpreted as a transitions from inelastic or brittle pro-
207 cesses (large scales) to plastic processes. This explanations is in agreement with
208 laboratory experiments that report that larger volumes of rock are, on average,
209 weaker ...

210 Fractal characterizations of surfaces do not uniquely define a profile or surface.
211 Other statistical metrics exist and are common place in many engineering practices.
212 Specifically, examining the statistical distribution of the height measurements of
213 a surface provides insight into the contact [?], frictional behavior [?] and wear
214 processes [?].

215 define skewness, kurtosis, etc.

216 The the statistical moment is defined as follows:

217 First ($m = 1$) and second ($m = 2$) order

218 **1.3 The evolution of slip surfaces with displacement**

219 Previous work has mainly focused on mechanical wear processes as the domi-
220 nant mechanism of surface evolution [?, ?, ?]. Mechanical wear processes include
221 any erosive process in which volume removal by abrasion, ploughing, and other
222 fracture-induced phenomena from surfaces in sliding contact. Before further ex-
223 ploring the effects of wear in fault slip surfaces, it is worth recognizing that many
224 other processes could—and likely do—cause the slip surface to evolve with displace-
225 ment.

226 A surface can change according to the following:

227 *surface deformation*

228 *Addition of material*

229 *Removal of material*

230 Fault slip surfaces have evidence pointing to each of these processes preserved
231 in the rock record.

232 *Surface deformation* encompasses any process by which a surface changes shape
233 by the rearrangement of material (no removal or addition of mass). Both elastic
234 and inelastic processes allow fault blocks on either side of a fault to deform. At
235 the seismic time-scales, only elastic and brittle deformation can occur—whereby
236 macroscopic fault damage and micro-fractures in grains and crystals away from
237 the fault can enable strain and dissipate stress on the fault. At longer time-scales,
238 calcite twinning, pressure solution, and clay alteration can also yield similar effects
239 through plastic deformation. These short and long-time scale mechanisms define
240 the visco-elastic rheology of fault blocks.

241 It is unlikely that the rheology of the fault block and its effect on the slip
242 surface topography are significant in the evolution of the slip surface. Using slick-
243 enline orientations and fault core thickness as a proxy to the fault block rheology
244 Kirkpatrick et al. 2014, find that 1) deformation does occurs in fault block and 2)
245 there is a scale dependence to this deformation. However, this scaling is not well
246 represented in fault geometric scaling. It would rather predict a change in scaling
247 at the outcrop scale. The absence of any such signal in the topography of fault
248 slip surfaces implies that deformational processes cannot directly determine how
249 slip surfaces evolve with displacement.

250 For its part, an *addition of material* occurs as fault rock is cemented onto slip
251 surfaces—filling in geometrical concavities and effectively reducing the amplitude

of surface irregularities. Its effect is preserved in the rock record with mobile, or *fluidized*, gouge cemented and re-fractured in subsequent faulting [?,?]. Moreover, it has been shown that discrete slip surfaces can form from the localization of shear strain within unconsolidated granular material (e.g. [?]). It is key to note that the effectiveness and rate at which this, and similar, mechanisms affect slip surfaces are then metered by the healing-rate and the wear-rate. These cannot be ruled out without new field investigation.

Removal of material is caused by mechanical wear. As fault blocks slide past each other, frictional wear is an inevitable process. Layers of comminuted fault rock, cemented or not, are direct evidence of this process [?,?]. Wear is known to be multiscale. At small scales, grains can be plucked or broken [?]; at larger scales grains plough slip surfaces to create corrugations [?] and sidewall ripouts form [?]. All these processes fall under the definition of wear in that they involve the failure of geometrical protrusions, only these are expressed at various scales. Moreover, these have substantive impact on the surface geometry.

MAKE FIGURE HERE FOR REFERENCE SIMILAR TO THE ONE IN YOUR EPSL SLICKENLINE/RHEOLOGY PAPER - but focus on the fact that there is an asperity failing.

While wear processes are subject of a vast field of research, particularly in engineering and tribology due to interest in manufacturing machine parts for longevity [?], its applications in the earth sciences is emergent with tests mainly conducted at laboratory scales [?,?,?,?]. The only application directly grounded with field data of natural fault surfaces is a prediction of wear volume presented in brodsky2011faults.

The wear rate, the volume of wear-product produced per unit offset is broadly

related to the real area of contact and loading. When two surfaces are put in direct contact, the real area of contact is much smaller than the nominal surface areas because the load is supported at microscopic protrusions from a surface, or *asperities* ([?, ?, ?, ?]). Remote loading normal to the surface causes local stresses and associated deformation at contact points. Note that as the load is increased, deformation of large asperities causes new asperities to come in contact. In its simplest form, wear rate ($\frac{\partial V}{\partial x}$) is defined according to defined to be proportional to the remote load (P):

$$\frac{\partial V}{\partial x} \propto P \quad (5)$$

The relation has been shown to be reasonably robust in experimentation for most materials. In further detail, the size, distribution and duration of contact areas, as well as the shape of the worn particles, control the general behaviour of wear. Note that material properties are contained in a constant of proportionality referred to as the probability factor—the probability of a collision of asperities to lead to removal of material [?].

Following this formulation, Scholz, 1987, proposed that wear rate for faults could be determined as a linear relationship with displacement and an inverse relationship with hardness. The displacement relationship is in reasonable agreement with laboratory experiments [?] and measurements of natural fault rock thickness [?, ?]. The hardness dependence is difficult to test given uncertainties in both fault rock thickness and hardness [?]. The simple formulation forwarded by Archard, 1953, and its application to faults by Scholz, 1987, was acknowledged to have serious limitations in their applications to natural faults. Specifically,

299 scholz1987wear raises concerns about the surface geometry of real fault, and about
300 the scaling and effectiveness of wear processes such as grains plucking and fault
301 rock abrasion.

302 Building off of experiments on engineering metals [?] and ceramics [?], new
303 fault wear model integrated a 'running-in' component which exponentially decays
304 towards steady-state [?, ?]. This behavior intruced a discrete such that the volume
305 of fault rock produced (V) can be expressed as a function of displacement (x)
306 according to:

$$V = \beta [1 - \exp(-nx)] + Kx \quad (6)$$

307 Where β , n , and K are constants.

308 A running-in stage is though to reflect effect of surface roughness. This later
309 formulations was supported by a semi-analytical formulations of asperity failure
310 and rotary shear experiments. However, in line with comments in Power et al.,
311 1988, we propose that this running-in stage on real faults is likely to be substan-
312 tially different for faults where fractal topography implies that new larger asperities
313 will come into contact with increasing displacement. Laboratory experiments have
314 limited fractal bandwidth. Shear boxes are limited to sample length; rotary shear
315 apparatus are limited to their circumference length. We highlight that wear pro-
316 cesses controlling the behaviour laboratory scale experiments are likely inadequate
317 for natural faults. These may instead reflect relict behaviour issuing from limited
318 fractal bandwidth and emplacement of mobile gouge layers buffering the surfaces.

319 It is clear that the fractal nature of fault surfaces is important to reconcile
320 with a model of wear. Concepts of fractal scaling, strength heterogeneity and

scale dependent strength are poorly captured by the current literature. Additional insight from field observations are needed to better understand fault slip surface processes. To date, notwithstanding preliminary efforts by Brodsky et al., 2011, linear scaling between fault rock thickness and displacement is nearly the only grounding field evidence for existing wear models (i.e. [?, ?, ?]). As pointed out by many authors [?, ?, ?] the scaling is contingent on highly uncertain and ambiguous measurements. Overlooking difficulties and/or inconsistencies in determining displacement, the representative fault rock thickness is difficult to measure given variations of in thickness (often many orders of magnitude, even for a single outcrop), inconsistent definitions of the measurements across the literature, and potential breaks in scaling for certain faults.

The lack of a model grounded in more field observations, quantitative data and theoretically consistent with our current understanding of fault slip surfaces is a blaring knowledge gap that we seek to fill in this study.

1.4 Faulting in Sandstone

Faults in the well sorted Navajo and Entrada Sandstones in the San Rafael desert provide an ideal natural laboratory for the study of fault maturation. These have correspondingly been subject of extensive study of fault mechanics (e.g. [?, ?, ?, ?, ?, ?, ?, ?, ?] [?]). Its is however important to recognize faulting in sandstones such as the Navajo and Entrada units do have some pecularitie that are worth outlining. Before presenting the tectonic and geological context of the the San Rafael desert, we first provide a brief overview of the existing litterature covering the nucleation, growth and coalescence of faults in sandstones with a specific focus on the areas

³⁴⁴ presented in this study.

³⁴⁵ Two fault nucleation models exist faults in sandstone [?, ?], the first model
³⁴⁶ is based on the localization of strain along deformation bands and deformation
³⁴⁷ band clusters. Deformation bands are a characteristic feature of high porosity
³⁴⁸ sediment [?, ?, ?]. Deformation bands define sinuous sheets which localise strain in
³⁴⁹ zones typically less than a few millimetres in thickness [?]. Strain is accommodated
³⁵⁰ by the run-away crushing of sedimentary grains and the concomitant collapse of
³⁵¹ pore space. Strain across deformation bands is typically in shear [?]. Shear strain
³⁵² accommodated across a single deformation band is typically on the order of mil-
³⁵³ limetres. With increasing shear strain, deformation bands coalesce in localized
³⁵⁴ zones called deformation band clusters. It is characteristic for deformation bands,
³⁵⁵ and deformation band clusters to protrude out of outcrop because of differential
³⁵⁶ weathering. Field studies show that faults form in or along these deformation band
³⁵⁷ clusters [?].

³⁵⁸ The second nucleation mechanism relies on the reactivation and coalescence of
³⁵⁹ regional mesoscopic joint sets [?, ?]. Subsequent deformation leads to the formation
³⁶⁰ of additional joints, sheared joints, zones of fragmentation, and, finally, through
³⁶¹ going slip surfaces enableb be the likage of splay fractures and joints (see figure [?]).
³⁶² This faulting mechanism is typically associated with more intense becciation and

³⁶³ The models have since been shown to be endmembers for the formation of faults
³⁶⁴ in the High porosity sandstone such as that of the Navajo Desert presented in this
³⁶⁵ study . Moreover, these mechanisms can act in unison and result in relatively
³⁶⁶ complex overprinted architectures [?].

³⁶⁷ The maturation of faults in the Navajo and Entrada sandstones, and similar
³⁶⁸ units in the region is particularly well recorded. In these units, the formation of

pristine, slickensided slip surfaces is common and seemingly does not require large displacement form [?, ?]. While the evolution of slip surface with displacement is not described in these field area (as will be done in this study), there has been substantial work describing the evolution and growth of damage zones with displacement which report roughly linear scaling laws over 0 to 50 meters of displacement [?, ?, ?]. Also, while it was typically thought that deformation bands pre-date the formation of faults [?, ?], it was shown that later generations of deformation bands also form as a fault damage feature. The spatial density of deformation bands and fault damage rapidly decreases with increasing distance from the fault according to a power law away from the center of the fault zone [?, ?]. The same field investigations reported no clear displacement scaling for fault core or fault rock over displacements ranging [?, ?].

1.5 Tectonic Setting

The San Rafael Desert hosts a sequence of gently dipping marine and sub-areal sedimentary rocks deposited from the Pennsylvanian to the Jurassic (see Figure 2). The San Rafael Desert is part of the San Rafael Swell, a monocline that formed when these sediments were uplifted as a passive drape fold above a reactivated basement reverse fault during the Late Cretaceous Laramide Orogeny [?, ?]. In turn, the swell is part of the broader Colorado Plateau [?]. Networks of joints and normal faults caused by Laramide activity cross-cut the sedimentary sequence and accommodate North-South extension [?, ?]. Within the San Rafael Swell, we focus the following field locations: 1) the Chimney Rock Fault Array (Navajo Sandstone) [?, ?, ?], 2) the Big Hole fault (Navajo Sandstone) [?, ?], 3) faults outcropped in

392 the Iron Wash (Navajo Sandstone) [?, ?] and 4) a network of deformation bands
393 and faults near Goblin Valley State Park [?, ?, ?, ?] (Entrada Sandstone) (see figure
394 XXX). Table ?? present detailed descriptions of the Navajo and Entrada sandstone
395 units.

396 Advantages of theses field locations are manifold. First, the nearly pure quartzite
397 lithology, extensional tectonic regime, depth (2-4 km or 40-80 MPa), temperature
398 (estimates range from 45-90 °C) of activity, and faulting mechanism are all rela-
399 tively consistent across all field areas [?]. Consistency in these parameters is key
400 to isolating the effect of displacement on the fault roughness and is missing in any
401 previous similar study of fault slip surfaces [?, ?]. Moreover, both field locations
402 exhibit well preserved fault surfaces that are exposed and accessible (see Figure
403 3).

404 The Chimney Rock fault array is an orthorhombic set of faults that crops out
405 at the northern end of the San Rafael Swell ([?, ?]). Two sets of oppositely dipping
406 normal faults crop out at the surface with preserved fault scarps. WNW-striking
407 faults have clear evidence for fragmentation and are aligned with pre-existing joints
408 and have correspondingly been interpreted to have formed by shear reactivation of
409 joints, conversely ENE-striking faults have relatively more abundant deformation
410 bands and show nearly no evidence of fragmentation and where therefore inter-
411 preted to have formed from deformation bands (Davatzes, 2003). Exposure is very
412 good, faults are abundant and have well preserved fault surfaces [?]. The Chim-
413 ney Rock fault array has studied to better understand of fault geometry [?, ?],
414 permeability [?] and kinematics [?, ?, ?, ?]. As a result, detailed maps of the fault
415 array have been produced (e.g. [?]) . In addition, by using measurements of the
416 separation between footwall and hanging wall cutoffs of sedimentary horizons,

417 entire displacement profiles have been measured for faults with a wide range of
418 displacements ([?, ?, ?, ?]). The Big Hole fault is located roughly 10 km to the
419 South-East of the Chimney Rock Fault Array. While not explicitly part of the
420 fault array, the Big Hole fault shares a nearly identical geological setting. The
421 Big Hole fault has been extensively studied in detail as an analog to hydrocarbon
422 reservoir-scale faults. Measurable displacements on the exposed fault range from
423 8 m to 39 m [?, ?].

424 Contrary to other field areas, Iron Wash, in the Navajo sandstone has not
425 featured a series of studies. However, it was mapped in detail by Aydin, 1977.
426 The area host a variety of normal, oblique and transform fault. Faults exposed
427 at Iron Wash are part of the Hawk's Nest fault system. The system has been
428 proposed to be related to the San Rafael Swell uplift [?]. Mapped displacement
429 range up to 80 m of offset. There are no large meters-scale slickensided surfaces.
430 However, it is possible to uncover small pristine slip surface sample on freshly
431 parted surfaces using a hammer and chisel. Here, displacement measurement are
432 readily obtainable by using the upper horizon of the Navajo sandstone, easily
433 distinguishable due to an disconformable contact also marked by a change in rock
434 color.

435 Large networks of deformation band faults outcrop near Goblin Valley State
436 Park on the southeastern margin of the San-Rafael Swell ([?]). This locality
437 comprises areas mapped in detail known as Molly's Castle and Horse Creek [?].
438 Because deformation bands dramatically alter the local permeability structure,
439 Goblin Valley has been extensively studied in light of fault nucleation and the im-
440 plications for hydrocarbon circulation (e.g. [?, ?]). At Goblin valley, deformation
441 band clusters outcrop in iconic centimeter- to meter-sized slabs. These are often

⁴⁴² bounded by discrete slip surfaces [?]. Offsets in sedimentary beds have allowed
⁴⁴³ previous studies to obtain detailed displacement measurements (e.g. [?]).

⁴⁴⁴ Together, these field locations offer the chance to survey well-preserved fault
⁴⁴⁵ surfaces that have hosted displacements from embryonic stages to 55 m of displace-
⁴⁴⁶ ment. Moreover, novel to this study, we are able to survey multiple expressions
⁴⁴⁷ of a single fault's surface with various displacements according the displacement
⁴⁴⁸ profile of the fault.

Table 1: Description of lithologies featured in this study [?]

	Navajo	Carmel	Entrada
<i>Age</i>	<i>Lower Jurassic</i>	<i>Middle Jurassic</i>	<i>Late Jurassic</i>
<i>Origin</i>	<i>Wind blown</i>	<i>Marine</i>	<i>Wind blown</i>
<i>Thickness</i>	$\sim 150\text{ m}$	$\sim 50\text{ m}$	$>150\text{ m}$
<i>Rock types</i>	<i>Sandstone, limey sandstone</i>	<i>Limestone, sandstone, siltstone, shale and Gypsum</i>	<i>Cross bedded sandstone, siltstone and shale</i>
<i>Composition</i>	$\sim 90\%$ quartz, 10% feldspar grains trace <1% ferromagnesia minerals calcite and silica cement		Quartz, feldspar and ferromagnesian minerals clay, calcite and quartz cement
<i>Mean Grain Size</i>	$\sim 0.05\text{ mm}$		$\sim 0.1\text{ mm}$
<i>Outcrop</i>	<i>Chimney Rock Big Hole Iron Wash</i>	<i>Chimney Rock</i>	<i>Iron Wash Molly's Castle</i>

Loca- tion	Lithology	Description	Displacement Constraints
Chim- ney Rock Fault Array	At the contact between the Navajo Sandstone and the base of the Carmel Unit	Orthorombic set of normal faults with preserved faults scarps of Navajo Sandstone	Displacement profiled of stratigraphic throw constrained by offset on a Carmel Limestone Marker Horizon by Maerten et al., 2000.
Big Hole Fault	Navajo Sandstone	One single large normal fault structure partitioning displacement on two major strands traceable for kilometers through a river wash with scarp exposure, and strike parallel/perpendicular cross-sectional exposure	Displacement constrained using the top Erosionally competent horizon at the top of the Navajo by Shipton and Cowie, 2003 and directly where possible.
Iron Wash	Navajo Sandstone	Network of normal and strike-slip cross-cutting faults. Little scarp exposure but has good cross-sectional exposure with fresh slip surfaces (using hammer and chisle)	Displacement mostly constrained by direct measurement of offset in the Upper Navajo horizon.
Molly's Castle	Entrada Sandstone	East-West striking network of normal faults and ubiquitous deformation bands. Well preserved slip surfaces broadly	Displacement constraints available in places from mapping by Aydin (1978) and directly measured using various marker

Table 2: Table caption

⁴⁵¹ 2 Objectives

⁴⁵² This study fills a fundamental knowledge gap in the field of structural geology
⁴⁵³ and earthquake mechanics. While it is increasing evident that fault roughness
⁴⁵⁴ is an important agent in the earthquake process, it is still unclear what defines
⁴⁵⁵ the magnitude and large spread in roughness of fault slip surfaces. To do so, we
⁴⁵⁶ test the two following hypotheses: 1) fault slip surface geometry is defined by its
⁴⁵⁷ displacement history wherein 2) wear is the dominant mechanism of slip surface
⁴⁵⁸ evolution.

⁴⁵⁹ These hypotheses are tested with three lines of inquiry:

- ⁴⁶⁰ 1. investigation of fault architecture and microstructure of faults in the San
⁴⁶¹ Rafael Desert, Utah (section ??). Observations have a specific focus on
⁴⁶² recording qualitative changes from zero displacements structures such as de-
⁴⁶³ formations bands and joints, to small displacement faults (centimeters of
⁴⁶⁴ displacements) and finally to larger faults (meters of displacement). We also
⁴⁶⁵ pay careful attention to the mechanisms that alter the slip surface geometry.
- ⁴⁶⁶ 2. geometric analysis of pristine fault surfaces preserved in the San Rafael
⁴⁶⁷ Desert , Utah, using scan data aquired in the field using a Lidar and a
⁴⁶⁸ laser scanner, and in the laboratory using white light interferometry (section
⁴⁶⁹ ??).
- ⁴⁷⁰ 3. numerical modelling failure of asperities using Boundary Element Modelling
⁴⁷¹ (BEM) applied to frictional faults in two dimension (Fric2D - [?, ?, ?, ?]) and
⁴⁷² crack growth by work-minimizations (GROW - [?]) (section ??).

⁴⁷³ Building upon the results from each component, we propose a wear model for

⁴⁷⁴ fault surfaces. This model calls upon scale dependent strength, strength hetero-
⁴⁷⁵ geneity and scale invariant asperity failure processes (section ??). Note that links
⁴⁷⁶ the scans of fault slip surfaces, Matlab scripts to process and analyse slip surfaces
⁴⁷⁷ and detailed documentation is available in the appendix.

⁴⁷⁸ **3 Field observations and Microstructure**

⁴⁷⁹ We first report on the architecture of faults cutting the Navajo and Entrada Sand-
⁴⁸⁰ stones with a specific focus on the evolution from zero-displacement structures
⁴⁸¹ such as joints and deformation bands to large offset structures with polished slip
⁴⁸² surfaces and accompanying fault rock lithologies.

⁴⁸³ **3.1 Zero-Displacement Structures**

⁴⁸⁴ The characteristics and surface morphology of the local zero-displacement fea-
⁴⁸⁵ tures are especially relevant to our analysis as they represent the initial, zero
⁴⁸⁶ displacement, roughness of faults in the study area. This is fundamental to
⁴⁸⁷ understanding the integrated maturation path of slip surfaces to larger displace-
⁴⁸⁸ ments [?].

⁴⁸⁹ **3.1.1 Deformation Bands and Deformation Band Clusters**

⁴⁹⁰ In outcrop exposure deformation bands are sinuous white lineaments. The sin-
⁴⁹¹ uosity and the variability thereof both are notably higher than that of faults.
⁴⁹² Accordingly, the trace of single deformation bands can be nearly as linear as small
⁴⁹³ faults; but can also form very arcuate paths. We note that isolated deformation
⁴⁹⁴ bands, far from faults, are typically less sinuous than those near faults and zones

495 of densely packed deformation bands. We observe a range in thickness for defor-
496 mation bands of 1 to 5 millimeters in thickness. Maximum observed shear offset
497 across a single deformation band is 10 cm but is more typically on the order of a
498 few milimeters. Corresponding maximum shear strain is on the order of 10, but
499 typically is on the order of unity as reported in flossen, 2007

500 Deformation bands often protrude out of outcrop as thin sheets (see figure
501 ??). The edges of the sheet are coated with single layer protolithic grain. A
502 faint anisotropy, whereby the dip-direction (parallel to strain) is smoother than
503 the horizontal direction (perpendicular to strain), is perceivable on the edges of
504 protruding deformation band sheets.

505 In thin-section, bands are associated with a gradational reduction in grains
506 size and an increase in angularity compared to the protolith (see figure ??). Along
507 with the reduction of grain size, intra-granular fracture are much higher, grains
508 are better packed and less porous.

509 Deformation band clusters contain groups, or clusters, of nearly co-planar, mu-
510 tually cross-cutting individual bands. The clusters are dense networks of anasta-
511 mozing deformation bands. The clusters range in thickness from a few millimetres
512 to tens of centimetres in width, often outcropping as slabs up to meters in height.
513 Clusters commonly form in upright conjugate pairs.

514 Deformation bands clusters have well defined edges. Given differential weath-
515 ering, particularly characteristic for the Goblin Valley area, deformation bands
516 form large meter-scale slabs. The exposed edges of deformation band clusters
517 have distinctly corrugated and "lumpy" morphology (see figure ??-left). The cor-
518 rugation is better defined than in individual deformation bands. The dip parallel
519 rake of the corrugations is in general agreement with the normal, dip-slip, local

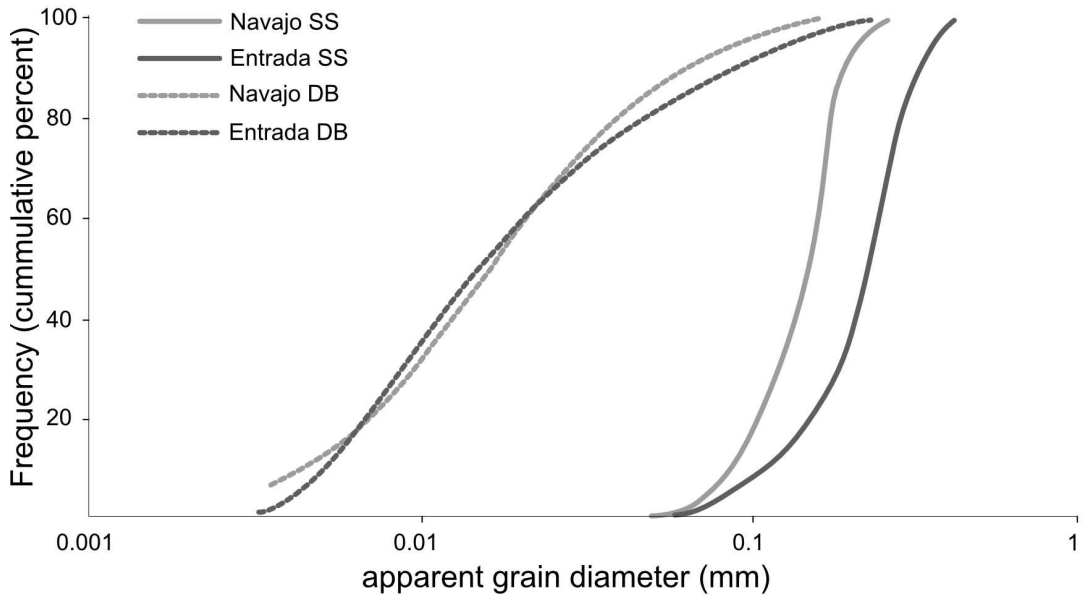


Figure 1: Grains size reduction of crushed grains within deformation bands relative to the undeformed sandstone units, the Navajo and Entrada sandstones. (figure adapted from Aydin, 1978)

kinematics. As is the case for individual deformation bands, edges of the deformation band clusters are always coated with a cohesive, single grain-thick layer of sand grains from the host sandstone. There is a clear directional asymmetry along the direction of shear whereby steep faces are in the direction of shear offset and shallowed faces are in the opposite directions (see figure ??). The asymmetry on the hanging-wall edges of the slabs is inverted on the foot-wall edges likely indicating an association with the overall kinematics of the clusters. Texture related to deformation band clusters are poorly captured in thin section because the size of any structural components exceeds the practical size of sections.

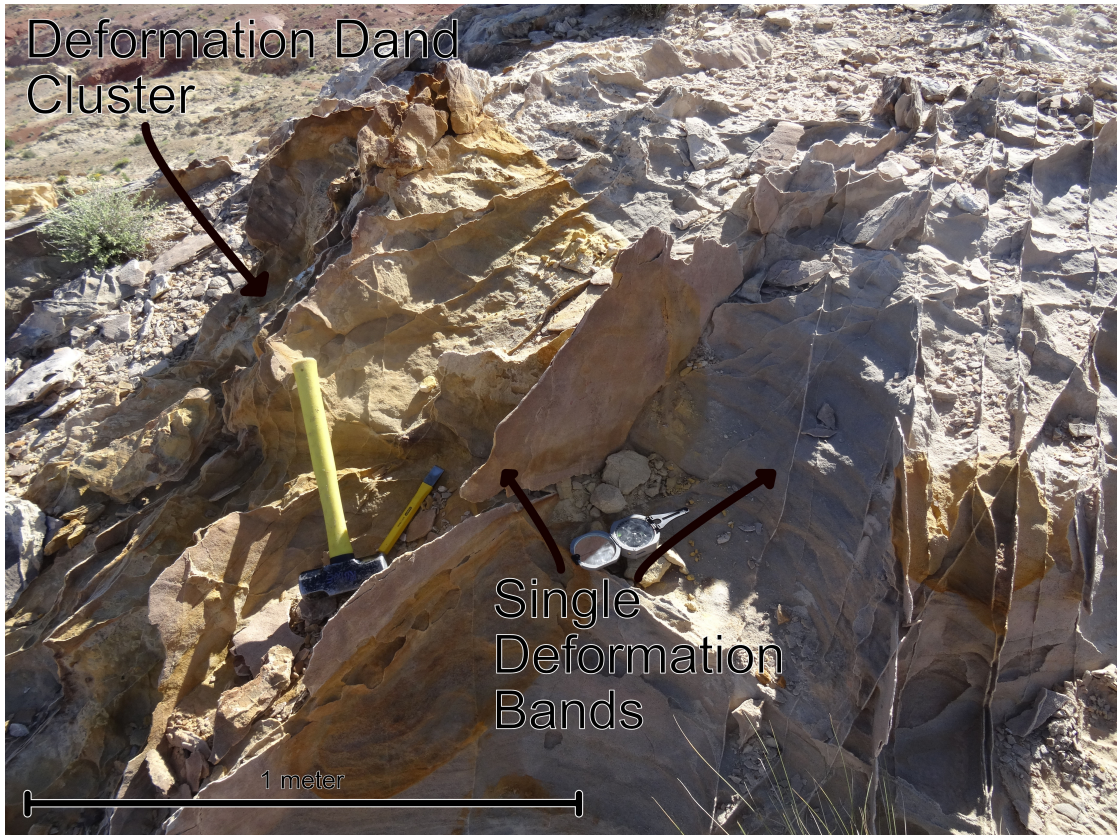


Figure 2: Example of single deformation bands protruding out of outcrop. A small deformation band cluster is also visible in the background.

529 **3.1.2 Joints**

530 Subvertical joints sets are a common feature of every locality. Joint sets are best
 531 defined in the upper Navajo units and lower Carmel limestone pavements. The
 532 abundance of joints increases near faults. Joints surface can be very large- effec-
 533 tively defining cliff faces 10's or even 100's of meters in size. Joints are better
 534 defined in the Navajo and Carmel Unit than in the Entrada. While spacing be-
 535 tween joint in the Carmel pavements is tight (on the order of 10 cm), the spacing
 536 in the Navajo appears to be much larger (1 m or more). Joint surfaces are notably
 537 smoother than deformation bands, but rougher than slip surfaces. Salient mor-

538 phological features on joint surfaces are the plumose structures relict from fracture
539 growth and fabrics aligned with cross-bedding horizons.



Figure 3: Left: Example of the edge of a deformation bands cluster at Molly's Castle. Note the "lumpy" morphology and an clear vertical directional asymmetry. Right: Cross-sectional view of a deformation band cluster with tens of centimeters of shear offset. It is unclear whether there is a through going slip surface localizing displacement. It is, however, definitely not on the edge of the cluster.

540 3.2 Slip Surfaces

541 Slip surfaces in the Navajo and Entrada sandstones are most readily identifiable
542 by their relatively planar and polished morphology with a reflective or even vitre-
543 ous polish. Striations and grooves on the slip surfaces mark the direction of slip.
544 In cross-sectional exposure, slip surfaces are discrete, through-going and smooth
545 relative to their zero-displacement counterparts. A sharp interface, separated by a
546 sub-mm thick layer of incohesive white powder bounded by two vitreous surfaces.
547 Thin milky white layers, less than a few centimetres in thickness, typically flank
548 slip surfaces. These are in turn, within dense network deformation bands. The slip
549 surfaces often cross-cut or bound deformation band clusters and the deformation
550 bands within them. Perpendicular profiles are notably more sinuous than slip par-
551 allel profiles. Slip surfaces are incohesive, and readily form a parting surface.(see

552 figure – figure similar to that in Jamies notes)

553 Slip surfaces are only preserved in the Navajo and Entrada Sandstones. For
554 example, in spite of good exposures in prospecting pits and careful inspection of
555 the slip zone, Navajo-Carmel contact at the Chimney Rock fault array does have
556 preserved slip surfaces in the Carmel Unit. It is unclear whether this indicates that
557 the Carmel units is more susceptible to erosion and/or alteration; or if a polished
558 finish is only a feature of the quartzite sandstones.

559 Thin section observations reveal a layered micro-structural architecture of the
560 faults rock locally bounding slip surfaces. The following succession, ordered ac-
561 cording to distance from the slip surface is typical for slip surfaces in sand stone: 1)
562 a very fine grained ultracataclastic layer, 2) a broader cataclasite layer (sometimes
563 absent) and 3) a deformation band zone, the density of which gradually decreases
564 into 4) the relatively intact protolith with disparate deformation bands.

565 The ultacataclasite is continuous, nearly always bounds the slip surface, and
566 ranges from sub-milimeter to 2 milimeters in thickness. Texturally, the layer tex-
567 turally overprints and cross-cuts all other layers. From visual assessment, the
568 grain size distribution has a steep but continuous (no clast/matrix distinction) fall
569 off with most grains being unresolvable at 400 fold magnification. Larger grains
570 do not exceed 10's of micron - significantly smaller than protolithic intact grains
571 which are on the order of 100's of micron. Grains have a large diversity in angu-
572 larity ranging from sub-rounded to angular. We were unable to find fragmented
573 counterpart within the ultracataclasite. This is indicative that the layer was likely
574 fluidized [?]. There are partially offset survivor grains which could be interpreted
575 as fragmented counterparts, however, these results from shear offset of fractures
576 through-going the entire unlacataclastic layer. These fractures and grains they

577 partially offset are instead indicative of cycling between healing and brittle failure
578 postdating the formation of the fluidized ultracataclastic layer. Ultracataclasite
579 layers preserve a faint, potentially compositional, foliation oblique to the fault.
580 Interpreted as S-type foliations, the kinematics from the flow banding are consis-
581 tent with sense of shear of grains protruding into the ultracataclasite and partially
582 sheared off. Previous work has shown no notable change in relative abundance of
583 major elements, silicon, calcium, potassium and sodium, of the undeformed sand-
584 stones [?]. We do however observe an increase in concentration in opaque oxides
585 near the slip surface.

586 Scattered Electron Microscopy (SEM) reveals

587 A sharp, irregular and discontinuous interface juxtaposes the cataclastic layer
588 to the ultracataclasite. The interface is characterized by a distinct difference in
589 grain size and spatial arrangement. Past this transition, grains are larger and
590 sometimes preserve damaged but intact sedimentary textures from the sandstone.

591 The interface between the ultracataclasite and the cataclasite is more irregular
592 than the slip surface. The irregularity is broadly associated with the following
593 two distinct length scales: the grain scale and the 'scalloping' length scale (see
594 figure ??). Grains at the interface are typically truncated such that their tops are
595 completely flattened. The transition towards flattened grains is well captured at
596 various different stages by instances where grains protruding into the ultracata-
597 clasite are still intact. ordered from least damaged to most damaged, we see the
598 following: 1) grains that protrude into the ultracatclasite with little to no damage
599 Other grains we evidence of healed internal cracks, 2) grains with various stages
600 of micro-cracking and fractures, with fracture orientations roughly parallel to the
601 slip and with some very small shear offset and, sometimes, rotation and 3) fully

602 cracked grain with the fragmented counterpart rotated along slip or completely
603 missing missing. While most of the fractures are only intra-granular, some frac-
604 tures can readily be projected into neighbouring grain.

605 A larger millimeter scale geometry can be traced from linking fractures. Both
606 ends of the fractures abut in the ultracataclastic layer with shallow obliquity (15°),
607 such that the crack follows an arcuate path with an overall 'scalloped geometry'.
608 The occurrence of these fractures seem to be anticorellated with the thickness of
609 the ultracataclasite. Again, this geometry is recorded at various stages ranging
610 from the alignements of multiple fractures within the catacla

611 In contrast to the ultracataclasite, the original grain geometry is sometimes still
612 discernible in the cataclasite. Grains size within the cataclasite layer is spatially
613 variable with bands or lens' of larger grains separated by finer, more angular grains.
614 These layers are texturally similar in overall geometry to deformation bands have
615 much smaller grains.

616 This cataclastic layer thickness is highly variable. It typically ranges from
617 millimetres to centimetres. Variability is directly associated with splay features
618 which intensify mechanical damage around the fault. Its thickness on either side of
619 the slip surface is often highly asymmetric. The layer is not always present. When
620 it is absent, the fault, still bounded by a thin ultracataclasite, directly transitions
621 into the intact host.

622 For certain faults, dark oxide filled fractures up to a few centimetres in length
623 abut steeply into the slip surface and over-print other fault-related textural fea-
624 tures. These are characteristically consistent with dynamics tensile cracks. If this
625 interpretation is correct, they would indicative of seismic rupture velocities.

626 The evolution of slip surfaces with displacement is qualitatively apparent.

627 Faults with small displacements (centimetres of offset) are distinctly different than
628 larger displacement faults (meters of offset). They are 1) visibly more sinuous, 2)
629 laterally discontinuous, 3) less polished, instead, having a dull lustre, and 4) not
630 bounded by well-defined gouge or cataclasites layers bounding the slip surface
631 visible in the field. The minimum observed offset across slip surfaces was approx-
632 imately 0.5 cm. It is unclear whether this lower bound is a mechanical transition
633 between deformation with deformation bands and slip on a discrete slip surface.

634 Our observations suggest that a single surface does not always accommodate
635 the bulk of the fault offset. Instead, fault zones often have many slip surfaces,
636 sheared joints and splays which partition offset.

637 Certain slip surfaces do accommodate the overwhelming majority of fault offset–
638 displacement accommodated by smaller neighbouring discontinuous slip surfaces
639 is minimal (Shipton, XXX). Based on observations from previous workers and
640 those made in this study where larger displacement slip surfaces are unambigu-
641 ously identifiable, we generalized the characteristics of large offset slip surfaces for
642 the Navajo and Entrada Sanstones as follows:

- 643 • *Large displacement slip surfaces are more discrete and planar.*
- 644 • *Larger displacement slip surfaces are not cross-cut by deformation bands or*
645 *more sinuous and discontinuous slip surfaces*
- 646 • *large displacement slip surfaces are nearly cohesionless and forming easy*
647 *parting surfaces*
- 648 • *Large displacement faults have a very vitreous finish;*
- 649 • *Large displacement slip surfaces are typically in the center of a damage zone.*

650 **Damage is an inevitable consequence of displacement and the ac-**
651 **companying mismatch that accumulates. Damage at the field locations**
652 **in this study is expressed as comminution (e.g. cataclasite and gouge),**
653 **fragmentation (e.g. breccia, splay joints) and shear deformation (specif-**
654 **ically deformation bands).**

655 In this study, we refer to *fault rock* as rocks associated with a fault (Snoke et
656 al. 1998). The faults in our study area display a very diverse range in fault rock
657 lithologies, ranging from fine-grained cataclasites to massive bodies of breccias (up
658 to meters of thickness).

659 Fault rock consistently bounds slip surfaces—often asymmetrically. However,
660 observations at the outcrop scale (10's of meters) both along the strike and dip
661 indicate that both the lithology and thickness of the fault rock are highly heteroge-
662 neous and are subject to large variability. These observations are consistent with
663 more detailed fault architecture mapping conducted by Shipton et el., 2002.

664 We do not observe a clear and tractable relation between fault slip surface
665 displacement and faults rock thickness. This is big part a result of difficulties in
666 defining a clear fault rock thickness criterion which well encapsulates the variety
667 of faults rocks – a challenge well highlighted in (Shipton et al., 2006).

668 * this stuff is left over's from editing and moving things around

669 Healed Gouges

670 - the spot at big hole

671 - iron wash (powder between the surface)

672 - micro-structure

673 - prospecting pit

674 - typically on thinned sections of the fault rock (near the slip surface) Catacl-

675 asites . . .

676 - big hole sample with slip surfaces on both sides of the cataclasite

677 - micro-structure - Breccias . . .

678 - thick sections of the Breccias occur lenses which range from cm's to meters in

679 thickness. Breccia clasts are typically poorly sorted and can be very coarse with

680 clast up to 10 cm in diameter. Clasts show indications for multiple generations

681 of brecciation.

682 Thin Quarts lens - iron wash

683 Systematic associations between fault rock and fault structure exist. For in-

684 stance, Davatzes et al., 2002 reports of a systematic association between the fault

685 rock lithology and the orientation of the fault set. Namely, the orthorhombic fault

686 set striking WNW has systematic association with fragmentation—fault breccias;

687 conversely the ENE fault set rather has slip surfaces cutting through deformation

688 band clusters (see figure ??). This relation was speculated to be the result of

689 contrasting genetic mechanism. The WNW set is the result of the reactivation of

690 regional joints. In contrast the ENE fault set is the the result of clustering and

691 anastamosing deformation bands acting as a catalysing agent to the formation of

692 a faults. In this study, we observe clear instance of lithological contacts being

693 associated with brecciation (photo at iron wash where the top of the Navajo is

694 brecciated and quickly reverts to a single fault strand. More over, large breccia

695 bodies are clearly related to points where faults are cross-cutting each other at

696 high obliquity as is often the case at the Chimney Rock fault array and

697 Complicating factors:

698 Associations between brecciation and lithological contacts . . .

699 Associations between brecciation and cross cutting faults . . .

700 For an extensive review and description of the faults in the Navajo and Entrada
701 sand stones refer to Aydin's thesis.

702 **3.3 Interpretation of field observations and roughness mea-
703 surements**

704 Cross-cutting relationships reported bot in this study and in previous work on
705 faults in the Navajo and Entrada units of the San-Rafael swell are particularly
706 informative. Large displacement slip surfaces are not cross cut by deformation
707 bands and more sinuous slip surfaces. However, large displacement slip surfaces
708 do cross-cut clusters of deformation bands and more sinuous slip surfaces. This re-
709 lationship is indicative of a clear evolution of the fault architecture by 1) localizing
710 displacement and 2) smoothing out slip surfaces.

711 Faults zones with larger offset are associated with larger damage zones and
712 more slip surfaces. This is particularly telling fact when with the observation that
713 small displacement slip surface do not cross cut larger displacement slip surfaces.

714 The cross cutting relationship implies that either slip either smaller less con-
715 tinuous slip surfaces pre-date the onset of the larger offset slip surface or that the
716 they splay off of it. However, we can reject the former as a possible mechanism as
717 it does not account for the increased density of slip surfaces on larger offset fault
718 zones. This implies that they either form directly from the stress heterogeneities
719 induced by the roughness of larger displacement slip surfaces.

720 Slip surfaces pre-dating large The former case stress heterogeneities from active
721 slip surfaces induced by fault roughness.

722 faults are smoother than joints or deformation bands

723 At the grains scale, grains are truncated, not ‘plucked’.

724 more linear fault traces where not offset by wavier fault traces

725 **The textural transition between the ultracataclasite and the catacl-**
726 **asite is best explained by dynamic grain size reduction and wear at the**
727 **slip surface interface producing ultracataclasite which overprint more**
728 **diffuse off-fault grain size reduction through grain crushing and defor-**
729 **mation band production.**

730 4 Geometric analysis

731 4.1 Method

732 Previous efforts to correlate fault roughness to displacement were frustrated by
733 limited cliff-size exposure and bad displacement constraints, fundamental to the
734 quantitative analysis of the roughness data (i.e. [?, ?, ?]). Field methods in this
735 study correspondingly prioritize 1) slip surface quality 2) good displacement con-
736 straints 3) the number of faults scanned. Note that we do not necessarily prioritize
737 large exposure size as has been done in previous work.

738 We collected high precision, high density measurements with optical scanners
739 in the field and, later, in laboratory on collected hand samples. Every scan was
740 associated with a constraint on displacement. Moreover, we also recorded the time
741 of day, location, quality of the slip surface, strike and dip of the fault slip surface,
742 slickenline rake, and both plan and cross-sectional photographs. When permitted
743 by outcrop exposure, we recorded an estimate of the fault rock thickness. See
744 appendix for the tabulation of this data. Together, all these measurements and

745 observations should provide the necessary data to robustly explain and quantify
746 the processes through which faults mature.

747 **4.1.1 Scan Data Acquisition**

748 A scan of a fault slip surface discretizes it into a *point cloud*, a series of x , y
749 and z coordinates. We measure slip surface roughness by analysing these point
750 clouds scans. Specifically, we average the slip parallel and perpendicular spectral
751 and statistical properties across hundreds of profiles. To ensure the fractal scaling
752 is well-captured by the point cloud data, we use the following three scanning
753 instruments capturing various scales of observations: a New View 8000 structure
754 image analyzer (Zygo Corporation), a NextEngine desktop laser scanner and a
755 BLAH BLAH LiDAR. Together, these instruments offer the potential to resolve
756 fault slip surface geometry with high accuracy and precision at over nine decades
757 of length scale.

758 *make a map of each areas with the location of every scan encoded with dif-
759 ferent symbols*

760 A light detection and ranging instrument was used to resolve length-scales
761 ranging from meters down to millimetres, (i.e. LiDAR). LiDar has been used in
762 many previous studies of fault roughness as it is easily deployable in the field and
763 provides rapid means to collet very large point cloud data set. However, its use is
764 limiting as it requires exceptionally good and, accordingly, rare exposure of fault
765 surfaces that are large enough and fresh enough to not have been degraded by
766 erosion. In this study, we report 5 ??? Lidar Scans (see figure).

767 The bulk of *in situ* field measurements were made at intermediate length-
768 scales ranging from centimetres down to hundreds of microns with the NextEngine

769 desktop 3D laser scanner. The NextEngine laser scanner has a working distance
770 of 13 to 57 cm. Maximum accuracy, point cloud density and resolution are all
771 broadly function of the working distance. In this study nearly all scan where
772 measure at the optimal minimum working distance (15 cm). Accordingly, point
773 clouds measured this study are expected to have an accuracy of 0.01 cm and a
774 point density of 41 540 points/cm². surface both to industrial-grade laser scanner
775 as reference. The scanner is not exactly built to be field ready. It requires a power
776 source, low light conditions, a stable surface to sit on, limited dust exposure and
777 must be connected to a computer. Therefore, to use the scanner in the field, we
778 connected both the laser scanner and laptop to a solar powered, *Goalzero* battery.
779 The scanner was encased and padded in a reinforced cardboard box cut such that
780 the depth exactly corresponds to the optimal instrumental depth of field. The set
781 up had the added advantage of being very portable, completely removing sunlight
782 and limiting dust exposure. We report 45 scans using this field apparatus.

783 Finally, hand samples were collected and at McGill laboratories using white
784 light interferometry. Slip surface samples are cut to be roughly 1 cm². We ap-
785 ply a 4 nm platinum coating. Point clouds where then produced using the New
786 View 8000 structure image analyzer (Zygo Corporation). The instrument is an
787 optical profilometer using a non-contact method, instead using a scanning white
788 light source. The profilometer can capture surface geometry over length-scales
789 ranging from millimetres down to hundreds of nanometres by using 2.5, 10 and 50
790 fold magnification objectives. Point point-clouds are relatively small, however it
791 is possible to seamlessly stitch smaller scans together. Point clouds where bench-
792 marked to a silicon carbide mirror reference. For the purpose of this study, all
793 samples where scanned at 20 and 2.75 magnification objectives. Scans obtained

794 at 20 fold magnification where stitched together to produce sections roughly 2 by
795 4 millimetres with over 10^7 points. Scans obtained at the 2.75 fold magnification
796 are typically on the order of the sample size and have 10^6 points. The later length
797 scale nicely bridges the interferometry and laser scanner spatial resolution. We
798 report on 73 point clouds obtained with the white light profilometer.

799 **We assess the effect of erosion of slip surfaces by qualitatively com-**
800 **paring freshly parted slip surfaces with fault scarps with surfaces that**
801 **have been exposed to the elements for a long time. Weathered scarps**
802 **do preserve slip surfaces. However, these have a reddish-brown to dark**
803 **tarnish and less vitreous lustres. Sections of the slip surface are plucked**
804 **off. Severely weathered scarps develop a slip perpendicular fabric as-**
805 **sociated with conjugate fractures and deformation bands abutting into**
806 **the slip surfaces. These surfaces where not scanned. From our field**
807 **observation, it is clear that erosion has the effect of re-roughening the**
808 **slip surfaces, especially at smaller scales. We can confidently attribute**
809 **these re-roughening effects to erosion because they did not occur in**
810 **freshly parted slip surfaces. The extent of weathering and erosion was**
811 **noted and taken into account in post-processing stage on data analysis.**

812 4.1.2 Constraining displacement

813 We associate every scan with displacement constraint. At The Chimney Rock
814 Fault Array and Big Hole Fault, entire displacement and/or throw profiles have
815 been measured during previous mapping campaigns ([?, ?, ?, ?]). For the Chimney
816 Rock fault array, we use geospatial data obtained from Maerten (personal com-
817 munications). At big hole we used maps in [?] as reference. At Iron wash, Horse

818 Creek and Molly's Castle, Atilla Aydin's mapping identified clear offset markers
819 where available ([?]). For these field locations we use maps available in [?]. When
820 necessary base maps for all field locations were digitized and georeferenced using
821 satellite images. Maps where all used the field to streamline scan data acquisi-
822 tion. Displacement were estimated after the field campaign using GPS locations
823 collected in the field. Additional measurements using basic tape measure and com-
824 pass triangulation methods where also obtained in the field to obtain true faults
825 slip surface displacement.

826 Base maps only report stratigraphic throw or, in some cases, offset across fault
827 zones. However, many slip surfaces, complex networks of deformation bands and
828 sheared joints which partition offset across fault zone (see figure). We there-
829 fore make a distinction between *offset* across an entire fault and *displacement*
830 across a single slip surface. Without good marker horizons and cross-sectional
831 exposure, how stratigraphic offset is partitioned across slip surfaces is ambiguous.
832 Offset across the entire fault zone therefore only serves as an upper-bound con-
833 straint on displacement across a single slip surface slip surface. For 60% of point
834 cloud measurements, this is the best available constraint on displacement.

835 We were able to reconstruct exact displacement in the following specific cases:
836 1) if cross-sectional exposure indicates only one slip surface; 2) If cross-sectional
837 exposure is good enough to clearly indicate cutoff surface (lamella, cross-bedding
838 or lithological contact); or 3) following [?] and, locally, [?], if it is unambiguous
839 that there is a *principle slip surface* accommodating the overwhelming majority
840 of fault offset, i.e. it is continuous, it has a layer of fault rock and is unmistakably
841 more linear and sharp than any other slip surface in the fault zone.

842 Errors on displacement estimates are either reported directly for previous work

843 when available. For Chimney rock, we report $1m$ precision based on high resolution
844 GPS mapping by Maerten et al., 2001. For Big Hole, we report $5m$ precision based
845 on total station surveying by Shipton et al., 2001. For our field measurements and
846 those made by Aydin, 1977, we report conservative 10% error on displacement
847 estimates.

848 **4.1.3 Scan data Processing**

849 We use point cloud spatial statistics to characterize and quantify features of the
850 topography that could record active surface processes on faults. We developed a
851 *MatLab* work flow to entirely automate data processing from the raw *.xyz* input
852 format to the final statistical analysis:

853 1. Preprocessing

- 854 (a) manual inspection and removal of coarsest defects in built in scanner
855 software
- 856 (b) export point cloud data to *.xyz* data
- 857 (c) Import *.xyz* data into *Matlab*
- 858 (d) Very coarse Height field filter (standard deviation threshold)
- 859 (e) Rotate mean plane to horizontal
- 860 (f) Orient grid along slip direction (using power spectral analysis)
- 861 (g) re-grid to even point spacing
- 862 (h) Remove defects
 - 863 i. Remove outliers in the height field (standard deviation threshold)

864 ii. Fractal model filter

865 iii. Remove re-gridding artefact

866 2. Processing

867 (a) Statistical analysis

868 i. Scale-dependent *RMS*

869 ii. Scale-dependent skewness

870 iii. Scale-dependent kurtosis

871 iv. Scale-dependent asymmetry

872 (b) Spectral Analysis

873 i. Fast Fourier Transform (FFT)

874 ii. Lomb-Scargle Periodogram

875 *make into figure, include bypasses and other recent additions*

876 Before conducting a statistical analysis scan data must be pre-processed into a
877 workable format. Scan data is a point cloud - a series of points with coordinates
878 x , y and z . Scans reported in this study typically have 10^6 to 10^7 points. In raw
879 form, the point clouds are randomly oriented, noisy and still contain instrumental
880 and physical artefacts. Physical artefacts include cracks, eroded sections, and
881 vegetation; instrumental artefacts include noise, smoothing and scattering. All
882 these features must be removed. The process of manual removal is labour intensive
883 and infeasible for a data set of the scope presented in this study. I rather opt to
884 automate this process. Only very large defects (defects that may substantially
885 effect the quality of finding a true mean plane) are manually removed.

886 The surface must first be rotated such that the mean plane is horizontal and
 887 aligned along slip. Linear trends in the data induce unwanted high frequency signal
 888 in data and also affect the quality of interpolation in upcoming steps. Thus, x , y ,
 889 z data is rotated around the axis \mathbf{u} determined by the normalized cross product
 890 between the normal vector to the mean plane of the point cloud, \mathbf{n} , and the unit
 891 vertical vector, \mathbf{n}_2 :

$$\mathbf{u} = \mathbf{n} \times \mathbf{n}_2 / |\mathbf{n} \times \mathbf{n}_2|$$

892 with the rotation,

$$R = \cos \theta \mathbf{I} + \sin \theta [\mathbf{u}]_x + (1 - \cos \theta) \mathbf{u} \otimes \mathbf{u},$$

893 were $[\mathbf{u}]_x$ is the cross product matrix of u and \otimes is the tensor product and \mathbf{I} is
 894 the identity matrix.

895 Fault surfaces are anisotropic [?]. The direction of slip is preserved in the
 896 anisotropy whereby the 'smoothest' direction is slip parallel and the 'roughest'
 897 direction is perpendicular to slip. The fault scan is rotated around the z axis such
 898 that the direction of slip is parallel to the x axis. The direction of slip is found by
 899 decimating raw data before performing spectral analysis along directions rotated
 900 by 1° increments around the z-axis, iterating through the steps of regridding at
 901 each rotation. In this radial search, roughness is quantified as the integral of the
 902 log-weighted power spectrum over the entire bandwidth of the sampled surface.
 903 The direction in which the roughness attains a minimum value is then identified
 904 as the direction of slip and subsequently used to rotated the original point cloud.
 905 The data is then interpolated onto a grid using a linear interpolation algorithm.

906 The point spacing of the grid is automatically defined by the point density over
907 the areal extent of the data:

$$\Delta x = N_{pts}/A \quad (7)$$

908 Where Δx is the point spacing, N_{pts} is the number of points and A is the
909 areal horizontal extent of the data. The later is determined using a convex hull
910 over the $x - y$ projection of the point cloud. This treatment results in the point
911 spacing of the grid to be roughly consistent with that of the original scan.

912 INCLUDE HISTOGRAMS FOR EACH FILTER

913 *Defects* include all physical surface features that are clearly not associated any
914 faulting process, *e.g.* cracks, eroded patches, vegetation, etc.. Defects are ideneti-
915 fied and filtered out using combination of thresholding methods. These methods all
916 involve identifying points or linear segments of points that are statistical outliers
917 to the distribution characterizing the entire surface.

918 The most aggressive filter implemented searches for outliers to the fractal
919 model. The filter removes entire linear segments of points with abnormally high
920 variance in the height field for the given scale of observation. For this implemen-
921 tation, I iterate over 10 filter segment length-scales. The length-scales are selected
922 using a log spacing between the 10 points and the length of the entire surface.
923 The threshold for segment removal is chosen to be four standard deviations from
924 the mean which accounts for < 0.1 percent of a normal distribution. Note that,
925 assuming a normal distribution of data for a given scale, the filter does not induce
926 a systematic bias in the mean value, since the filtering is symmetric around the
927 mean. However, surface features associated with a truly distinct mechanism of for-

928 mation, in this case cracks and other defects that will typically have much higher
929 variance, *are* be removed. This general approach ensures that defects, regardless
930 of their scale are identified and removed.

931 In some cases, abnormally flat sections are introduced into a surface height
932 field during the interpolation of sparse points. Typically, interpolation on the
933 edge on a non-convex set of points is subject to this effect. These artefacts are
934 readily identified following calculation of the surface curvature data. In the log-
935 transformed absolute value curvature field, these sections appear to be nearly or
936 exactly zero. The filter rejects point with curvatures less than $10^{-25}m^{-1}$. These
937 values are assumed to be the result of the linear interpolation scheme.

938 Finally, all scan are inspected to make sure that the pre-processing was suc-
939 cessful. The workflow fails to properly process scans that have too many defects
940 surface defects. This is because 1) the mean plane is skewed by surface defects
941 and in turn affects identifications of outliers in the height-field; and 2) the dis-
942 tinction between the fault surface and outliers becomes less distinct in the fractal
943 model. These scans were manually cleaned and oriented before re-processing them.
944 Manual changes were executed in a point cloud editing software *CloudCompare*.

945 Pre-processed scans are N by M scalar fields of fault surface topography(the
946 sitance from the mean plane) aligned with slip along the x axis. NaN values mark
947 locations where data is missing or was removed by filters. Point spacing is defined
948 the mean point density of the scan in the x - y plane.

949 We adapt the general pre-processing workflow to account for instrumental arte-
950 facts. Scans collected with the LiDAR required more extensive manual point re-
951 moval to avoid features such as vegetation, spurious outlier and large defects to
952 affect the quality of the preprocessing. Scans collected at the intermediate scale

953 with the laser scanner easily followed this workflow. Finally, scan collected with
954 the white light interferometer have little to no surface defects and are aligned
955 before scanning. Moreover, instrumental *Zygo* software automatically generates
956 point clouds in grid-form. Therefore, for these scans, most of the pre-processing
957 step are omitted.

958 **4.1.4 Statistical Analysis**

959 After pre-processing, scans discretize defect-free slip surfaces with grids with rows
960 aligned with the slip direction. We compute the power spectral density content for
961 every continuous segment of every single profile of the grid using a Fast Fourier
962 Transform (FFT). Individual spectra are interpolated onto a master frequency
963 vector. For a given frequency, the distribution of power values across the pro-
964 files through along the slip is strongly skewed (see figure xxx). The skewness is
965 attributable to the non-negative constraint on power and residual outlying pro-
966 files (defects not properly removed). To provide a more representative and robust
967 measure of maximum likelihood, we use the geometrical mean instead of the arith-
968 metical mean. Accordingly, errors represent the 1σ range in the log-transformed
969 distribution. The analysis yields one representative spectrum for each scan.

970 The spatial frequency content of slip surfaces follow a power law. This charac-
971 teristic is roughly fixed for a single slip surface regardless of the scale sampled in
972 our instrumental array. Fixed scaling and its power law form in frequency space is
973 a feature of the fractal character of fault surfaces. We can thus further distil the
974 roughness measurements using the fractal model of the fault:

$$P(k) = Ck^{-\beta} \quad (8)$$

Accordingly the entire spectral information of a scan can be summarized with the prefactor (C) and the scaling exponent (β). Determining fractal parameters from spectra is not trivial. *A priori*, the fractal model is determined using a weighted power law regression through the spectra. Weights are determined according to the inverse $1\sigma^2$ variance of the power estimates. However, confidence interval on the fit parameters are strongly sensitive to both instrumental and analytical biases (XXX schittbulh 1998). Biases induce unwanted high or low pass filters in the spectral content-amplifying or diminishing selective bandwidth. The combination of instruments and highly overlapping bandwidths provides a means to identify the affected sections and suppress methodological bias. The comparison of the power law fit through multiple heavily overlapping instrumental bandwidths to the representative spectral of individual scans highlights instrument-specific biases. In doing so, we identify conservative bounds on sections of frequency spectrum that deviated from the power law fit. For our instruments, we find that artefacts are particularly disruptive at the small scale instrumental limit. The LiDar and laser scanner are dominated by a shallower slope at the high frequency tail of the spectra which has been interpreted in previous studies as random noise (XXX). Conversely, the spectra of the scan collected using the white light interferometer have steeper high frequency tails. This artefact has not been reported in previous studies in spite of the extensive use of the instrument. This discrepancy is likely attributable to the comparatively limited and subdued use of aggressive smoothing filters both in the scan data and in the spectra our analysis. Affected bandwidths are omitted from subsequent analysis. In spite of this approach, small discrepancies in parametrization of the power law fit for a given slip surface render the extrapolation of measurements from on instrumental bandwidth to the other

1000 instrumental scale of limited use. We therefore choose to report any further re-
1001 sults at the bandwidth or specific wavelength best captured by the instrumental
1002 magnification.

1003 INCLUDE A FIGURE WITH: ORIGINAL SURFACE, AUTOMATICALLY
1004 PROCESSED GRID, MANUALLY PROCESSED GRID AND CORRESPOND-
1005 ING POWER SPECTRA.

1006 identifying fractal scaling section plot of white light all magnifications compu-
1007 tational scheme to select the good section error on direct displacement estimates?

1008 **4.2 Results**

1009 **4.2.1 Roughness measurements**

1010 figures to :

- 1011 • all spectra
1012 • increasing anisotropy (two surfaces) - polar plot

1013 Figure XXX shows the all the PSD calculations obtained from the scans col-
1014 lected in this study. Consistent with previous work, we find that the PSD spectra
1015 over the entire bandwidth reported in this study generally follow a power law scal-
1016 ing (a linear relation in log-log space). This feature corresponds to the constant
1017 fractal scaling. The scaling exponent and pre-factors are calculated using linear
1018 least-squares fit of the spectra in log-log space. The Hurst exponent can then be
1019 obtained according to equation XXX.

1020 In the slip perpendicular direction, Hurst exponents range from XXX to XXX,
1021 with an average value of 0.8ish; Prefactors range from XXX to XXX with an

average value of XXX. In the slip parallel direction, Hurst exponents range from XXX to XXX, with an average value of 0.8ish; Prefactors range from XXX to XXX with an average value of XXX. Implicit to the pre-processing grid alignment, for any single scan the slip parallel direction is systematically smoother than the slip perpendicular direction indicating a clear surface anisotropy. The entire data set does however indicate an overlapping range in slip parallel and perpendicular directions. We also note that lower pre-factors are generally associated with lower Hurst exponents.

An evolution with displacement is weakly expressed in the spectral analysis but is cluttered and obscured by highly variable errors on displacements and roughness measurements. In order to highlight the effect of displacement on the surface roughness, we separate our scan data into two distinct populations. 1) Scan data with direct displacement constraint and 2) scan data associated with maximum displacement constraints. Brodsky et al., 2011, tested the validity of a power law relation between fault roughness at various specific scales and displacement. Building upon this approach, we use both data populations to test the validity and parametrization of the fit and the Implicit hypothesis that faults smooth as a function of displacement—the smoothing model. Scan data with direct displacement constraints serves as a direct test and a means to parametrize the smoothing model. For the model to be valid it must agree with further constraints imposed by data with only maximum displacement estimates.

A point defined by the maximum error bound on displacement and the roughness of the fault surface is in agreement with smoothing model if it is rougher than roughness prescribed by the model as parametrized by direct measurement. Conversely, if the point is rougher than the model prediction, it is not physically

1047 possible in the model construct. A null hypothesis would prescribe no bound on
1048 the roughness and would simply have the predicted roughness of a fault be defined
1049 by the probability distribution function of the entire roughness dataset.

1050 * probably will revisit this *

1051 Accordingly, we can roughly estimate the probability that our distribution of
1052 data relative to the smoothing model is a random element of chance according to:

$$P = \prod p(y_i > Y(x_i)) \quad (9)$$

1053 Figure shows the relation between roughness and displacement as interpolated
1054 a various scales of observation. Vertical error bars on the power spectral density
1055 are obtained from the confidence interval of the of the fractal model regression.
1056 Horizontal errorbars on displacement are defined on a case by case basis from
1057 field observations and previous work in on the fault arrays. We present both
1058 the fit through the our entire dataset (comprised of direct and upper bound con-
1059 straints on displacement) and through the the directly constrained displacement
1060 estimates. Fits are obtained using a least squares linear regression through the
1061 log-transformed data sets. In order to provide error bounds on the fit parameters,
1062 we use a full Monte Carlo simulation sampling direct displacement estimated as
1063 Gaussian distributions, upper bound displacement constrains as completely ran-
1064 dom distributions across the entire possible range of displacements and power
1065 spectral density estimates as log normal distributions. Errors represent on stan-
1066 dard deviation estimated from 10000 simulations.

1067 The weak trend across the entire dataset imply and expectation of smoother
1068 slip surfaces in fault zones which have accommodated larger displacement.

1069 Conversely the stronger trend across the well constrained data implies that an
1070 individual slip surface smooths with displacement. The smoothing exponent varies
1071 according to the different scales of observation (XXX at the laser at the centimeter
1072 scale, XXX at the millimetre scale and XXX at the micron scale). While a power
1073 law fit to the best constrained measurements is has poor fit metrics, we find a nearly
1074 perfect agreement with roughness measurements only associated with upper bound
1075 constraints.

1076 Two constraints on displacement – two data populations plot of all the spectra
1077 color coded with displacement smoothing plots: parallel - ζ all scales perpendicular
1078 - ζ all scales Hurst exponent - ζ all scales Fit for smoothing through direct data,
1079 discuss consistency with max disp data Other statistical metrics? Poly-gaussian
1080 features in the surface roughness Skewness of height field as a function of scale
1081 Null result worth reporting? Do a plot of the evolution of skewness at the grain
1082 scale?

1083 qualitative illustration of maturity

1084 4.3 Hard facts

1085 The following is a list of ‘hard facts’ that can be established from the both the
1086 qualitative and quantitative data:

- 1087 • faults are smoother than joints or deformation bands
 - 1088 – power spectrum shows that fault slip surfaces are systematically smoother
1089 than joint and deformation band surfaces at all wave lengths reported
1090 in this study (10^{-6} to 10^5 meters)
- 1091 • At the grains scale, grains are truncated, not ‘plucked’.

- The roughness of a slip surface is sensitive to its displacement history. This result is robust across multiple faults both nucleated from deformation bands and joints and variations in fault rock and host rock lithology.
- The smoothing exponent is likely more than 1 at certain scales - quote from Emily: "In all of these cases, the scatter of the data is large, but the basic result holds: the absolute value of the exponent is much less than 1."
- The smoothing rate is highest at small displacements and decreases with displacement.
- Smoothing occurs at all scales of this study
 - a slip surface from a large offset fault is more likely to be smoother
 - for any given the displacement on a fault, the smoothest slip surface roughly follows the same smoothing trend as that defined by direct displacement measurements.
- The roughness varies spatially on a slip surface - the scatter in the data exceeds the instrumental error
- the height distribution of points on a slip surface can be far from normally distributed.
- the Hurst exponent has a very large range in values (less than Zero to 0.9)
- more linear fault traces where not offset by wavier fault traces

₁₁₁₁ **5 Model**

₁₁₁₂ In this study, we utilize work minimization and boundary element numerical mod-
₁₁₁₃ elling to capture the growth of fault damage and the effect of rough asperities.
₁₁₁₄ The modelling component is motivated by the following questions: can geomet-
₁₁₁₅ rical asperities fail through shear? In so doing, how do they fail?—and what are
₁₁₁₆ its sensitivities to asperity geometry and strength? Does strength heterogeneity
₁₁₁₇ and mechanical wear by the truncation of asperities properly capture the evolu-
₁₁₁₈ tion of fault slip surfaces with displacement. These questions prompt the need for
₁₁₁₉ physically robust models that can be accomodating of complex fault or asperity
₁₁₂₀ geometries. The complexity of these geometries imply that off fault damage will
₁₁₂₁ grow in complex stress conditions— conditions that are currently poorly captured
₁₁₂₂ by simple analytical solutions (e.g. [?]). Moreover, complexities related to the
₁₁₂₃ discontinuous nature of fracture are more simply captured by boundary element
₁₁₂₄ modelling than existing finite element or finite difference models. This simplicity
₁₁₂₅ arises from need of fewer, less sparse, sets of equations to solve ([?]). Limita-
₁₁₂₆ tions of the boundary elements approach for fault modelling and off fault damage
₁₁₂₇ predictions is the difficulty of accumulating offset. Maximum allowable offset is
₁₁₂₈ roughly half the length of boundary elements. Along with this complications is the
₁₁₂₉ implicit trade off between model resolution and displacement. Approaches can be
₁₁₃₀ taken to circumvent the challenge however its development and implementation
₁₁₃₁ are beyond the current scope of this study.

₁₁₃₂ The model builds off of fric2D and growth by optimization of work (GROW)
₁₁₃₃ developed by Michele Cooke and Jessica McBeck. Fric2D solves for displacement
₁₁₃₄ and stress conditions on fault elements with prescribed constitutive behaviours

given prescribed boundary element stress boundary conditions and material properties in two dimensions. Constitutive behaviour of fault elements are defined by its static and dynamic friction, critical slip distance, and shear and normal stiffness. In turn the behaviour of the medium fault elements and boundary elements is linear elastic defined by Poisson's ratio and Young's modulus. For its part, GROW predicts fracture propagation paths. It does so by minimizing the external work on a system. As a natural analogue, the external work is the tectonic work imposed on a fault and its fault blocks, together comprising the system. The model allows for the simultaneous growth of multiple fractures. The general algorithm uses the same boundary element method as fric2D to describe the fractures–linear dislocation elements that discretize the entire length of the fault. As a crack grows, dislocation elements are added radially to the tip of the crack so as to minimize the external work on the system normalized by the crack area ($W_{ext}/\Delta A$). External work is further defined as:

$$W_{ext} = \oint (\tau u_s + \sigma_n u_n) dB \quad (10)$$

External work is readily calculated from the output of fric2D. Accordingly it is possible to iteratively test a range of directions of growth, compare the external work required, and choose the energetically preferred direction of crack growth. This process continues until stress at the tip of the cracks is not sufficient to overcome the fracture toughness. Therein lies the general algorithm of GROW.

In practice GROW utilizes almost the same inputs as fric2D. The user must specify what points are considered to be 'flaws'. Only the coordinates associated with the flaws are analysed and allowed to grow according to the GROW algorithm.

1157 The computational cost of multiple initiation points is large. Every added flaw
 1158 grows the computational cost exponentially according to the angular range and
 1159 resolution. We rather use fric2D to educate the choice of coordinated for the flaws
 1160 on the fault.

1161 Stress conditions are assessed along the fault elements. Normal (σ_{11}), shear
 1162 ($\sigma_{12} = \sigma_{21}$) and tangential (σ_{22}) stresses on the fault elements yield the two di-
 1163 mensional stress tensor. Its Eigenvalues in turn allow for the determinations of
 1164 principle stresses (σ_1 and σ_3). These in turn allow for calculation of the Mohr
 1165 Coulomb stress and the assessment of elements prone to failure in shear according
 1166 to host rocks angle of internal friction (ϕ) and cohesion (c).

$$\tau_m = \sigma_m \sin(\phi) + c \cos(\phi) \quad (11)$$

1167 where,

$$\tau_m = \frac{\sigma_1 - \sigma_3}{2} \quad (12)$$

1168 and,

$$\sigma_m = \frac{\sigma_1 + \sigma_3}{2}. \quad (13)$$

1169 We also assess element that may fail in tension. Elements with least principle
 1170 stress in tension exceeding the cohesive strength of the medium are also identified
 1171 as being prone to fail. In the likely case that entire fault segments (multiple fault
 1172 elements) are in stress conditions exceeding the failure criterion of the rock, we
 1173 choose local maxima of Coulomb stress and tensile stress along these segments as
 1174 the failure points.

1175 This additional functionality is implemented in Matlab and seamlessly links
1176 fric2d, failure assessments and GROW into one single workflow.

1177 **5.1 Model Results**

1178 **6 Discussion**

1179 **6.0.1 Tying the model together with roughness measurements and**
1180 **model**

1181 wear rate (character), tying together model with

1182 **6.1 An external estimate of gouge production and fault**
1183 **thickness * this section will likely be removed**

1184 The data collected in this study offers the unique opportunity to provide new
1185 indirect estimates of fault rock production, fault thickness and dilation rate over
1186 an entire fault. We know that 1) the primordial roughness is systematically rougher
1187 than mature faults, 2) the primordial roughness is relatively constant, and 3) the
1188 roughness can be estimated for a given displacement. Using these results, I will
1189 estimate the volume of fault rock produced through wear and the corresponding
1190 roughness induced accommodation space in the fault system.

1191 Displacing two rough fractal surface in shear requires dilation. The expectation
1192 dilation can be estimated according to the amplitude of the largest wavelength (λ)
1193 being offset (see figure XXX). For a given displacement, u , the largest wavelength
1194 in the system will be $\lambda = 2u_i$. Using a fractal paradigm to define the average
1195 amplitude of a given wavelength according to the pre-factor β and the Hurst

₁₁₉₆ scaling exponent, H , (*reference the equation*) we find that the dilation, A can
₁₁₉₇ be expressed as a function of displacement:

$$A(u) = \sqrt{\beta 2u^{-2H-1}} \quad (14)$$

₁₁₉₈ If we apply this to an entire fault system with displacement field, U , we can
₁₁₉₉ estimate the void space that would be produced:

$$V_{void}(U) = \int_S \sqrt{\beta 2U^{-2H-1}} dS \quad (15)$$

₁₂₀₀ Since the fault system is closed any change in fault roughness *must* be coupled
₁₂₀₁ to the fault core. If all changes in the fault surface are associated with a production
₁₂₀₂ of fault rock, we can effectively estimate the volume of fault rock that has been
₁₂₀₃ produced from displacement u_0 to u_f by comparing the volume integral under the
₁₂₀₄ corresponding initial and final slip surfaces $S(u_0)$ and $S(u_f)$.

$$\frac{\Delta V_{faultrock}}{\Delta u} = \int_S S(u_0) - S(u_f) dS \quad (16)$$

₁₂₀₅ volume integral under the surfaces, S , can be estimated numerically according
₁₂₀₆ to the frequency distribution prescribed by the RMS the entire fault system. Note
₁₂₀₇ that the RMS is estimated at the length scale of the entire fault; wear processes
₁₂₀₈ are active at all length scales below this.

$$\int S dS \approx \quad (17)$$

₁₂₀₉ Now for the displacement field, U , we can estimate the total fault rock produced
₁₂₁₀ by using the primordial surface roughness, $S(0)$, and the prediction of the surface

1211 roughness extrapolated to the length of the fault (* reference the the equation of
1212 smoothing *) such that:

$$V_{faultrock}(U) = \int_S S(0) - S(U) dS \quad (18)$$

1213 The comparison between the two quatities is telling. If the amount of fault
1214 rock is

1215 7 conclusion

1216 7.1 future work

1217 References

- 1218 [1] Keiiti Aki. Asperities, barriers, characteristic earthquakes and strong motion
1219 prediction. *Journal of Geophysical Research: Solid Earth*, 89(B7):5867–5872,
1220 1984.
- 1221 [2] JeFoa Archard. Contact and rubbing of flat surfaces. *Journal of applied
1222 physics*, 24(8):981–988, 1953.
- 1223 [3] CA Aviles, CH Scholz, and John Boatwright. Fractal analysis applied to
1224 characteristic segments of the san andreas fault. *Journal of Geophysical
1225 Research: Solid Earth*, 92(B1):331–344, 1987.
- 1226 [4] Atilla Aydin. *Faulting in sandstone*. PhD thesis, Stanford, 1977.

- 1227 [5] Atilla Aydin and Arvid M Johnson. Development of faults as zones of defor-
1228 mation bands and as slip surfaces in sandstone. *Pure and applied Geophysics*,
1229 116(4):931–942, 1978.
- 1230 [6] Nir Badt, Yossef H Hatzor, Renaud Toussaint, and Amir Sagy. Geometrical
1231 evolution of interlocked rough slip surfaces: The role of normal stress. *Earth*
1232 and *Planetary Science Letters*, 443:153–161, 2016.
- 1233 [7] Philip Berger and Arvid M Johnson. First-order analysis of deformation of
1234 a thrust sheet moving over a ramp. *Tectonophysics*, 70(3-4):T9–T24, 1980.
- 1235 [8] RL Biegel, W Wang, CH Scholz, and GN BorrNoTr. 1. effects of surface
1236 roughness on initial friction and slip hardening in westerly granite. *Journal*
1237 of *Geophysical Research*, 97(B6):8951–8964, 1992.
- 1238 [9] Andrea Bistacchi, W Ashley Griffith, Steven AF Smith, Giulio Di Toro,
1239 Richard Jones, and Stefan Nielsen. Fault roughness at seismogenic depths
1240 from lidar and photogrammetric analysis. *Pure and Applied Geophysics*,
1241 168(12):2345–2363, 2011.
- 1242 [10] Tom G Blenkinsop. Thickness—displacement relationships for deformation
1243 zones: Discussion. *Journal of Structural Geology*, 11(8):1051–1053, 1989.
- 1244 [11] Elisabeth Bouchaud. Scaling properties of cracks. *Journal of Physics: Con-*
1245 *densed Matter*, 9(21):4319, 1997.
- 1246 [12] Frank Philip Bowden and David Tabor. *The friction and lubrication of solids*,
1247 volume 1. Oxford university press, 2001.

- 1248 [13] Emily E Brodsky, Jacquelyn J Gilchrist, Amir Sagy, and Cristiano Collettini.
1249 Faults smooth gradually as a function of slip. *Earth and Planetary Science*
1250 *Letters*, 302(1):185–193, 2011.
- 1251 [14] Emily E Brodsky, James D Kirkpatrick, and Thibault Candela. Constraints
1252 from fault roughness on the scale-dependent strength of rocks. *Geology*,
1253 44(1):19–22, 2016.
- 1254 [15] Stephen R Brown and Christopher H Scholz. Broad bandwidth study of the
1255 topography of natural rock surfaces. *J. geophys. Res.*, 90(B14):12575–12582,
1256 1985.
- 1257 [16] Roland Bürgmann, David D Pollard, and Stephen J Martel. Slip distribu-
1258 tions on faults: effects of stress gradients, inelastic deformation, heteroge-
1259 neous host-rock stiffness, and fault interaction. *Journal of Structural Geol-*
1260 *ogy*, 16(12):1675–1690, 1994.
- 1261 [17] J Byerlee. Friction, overpressure and fault normal compression. *Geophysical*
1262 *Research Letters*, 17(12):2109–2112, 1990.
- 1263 [18] Jonathan Saul Caine, James P Evans, and Craig B Forster. Fault zone
1264 architecture and permeability structure. *Geology*, 24(11):1025–1028, 1996.
- 1265 [19] Thibault Candela and Emily E Brodsky. The minimum scale of grooving on
1266 faults. *Geology*, 44(8):603–606, 2016.
- 1267 [20] Thibault Candela, François Renard, Michel Bouchon, Alexandre Brouste,
1268 David Marsan, Jean Schmittbuhl, and Christophe Voisin. Characterization
1269 of fault roughness at various scales: Implications of three-dimensional high

- resolution topography measurements. *Mechanics, Structure and Evolution of Fault Zones*, pages 1817–1851, 2010.
- [21] Thibault Candela, François Renard, Michel Bouchon, Jean Schmittbuhl, and Emily E Brodsky. Stress drop during earthquakes: effect of fault roughness scaling. *Bulletin of the Seismological Society of America*, 101(5):2369–2387, 2011.
- [22] Thibault Candela, François Renard, Yann Klinger, Karen Mair, Jean Schmittbuhl, and Emily E Brodsky. Roughness of fault surfaces over nine decades of length scales. *Journal of Geophysical Research: Solid Earth*, 117(B8), 2012.
- [23] Thibault Candela, François Renard, Jean Schmittbuhl, Michel Bouchon, and Emily E Brodsky. Fault slip distribution and fault roughness. *Geophysical Journal International*, 187(2):959–968, 2011.
- [24] G Chambon, J Schmittbuhl, A Corfdir, N Orellana, M Diraison, and Y Géraud. The thickness of faults: From laboratory experiments to field scale observations. *Tectonophysics*, 426(1):77–94, 2006.
- [25] FM Chester and JM Logan. Implications for mechanical properties of brittle faults from observations of the punchbowl fault zone, California. *Pure and Applied Geophysics*, 124(1-2):79–106, 1986.
- [26] FM Chester and JM Logan. Composite planar fabric of gouge from the punchbowl fault, California. *Journal of Structural Geology*, 9(5-6):621IN5–634IN6, 1987.

- 1292 [27] Frederick M Chester and Judith S Chester. Stress and deformation along
1293 wavy frictional faults. *Journal of Geophysical Research: Solid Earth*,
1294 105(B10):23421–23430, 2000.
- 1295 [28] Frederick M Chester, James P Evans, and Ronald L Biegel. Internal structure
1296 and weakening mechanisms of the san andreas fault. *Journal of Geophysical*
1297 *Research: Solid Earth*, 98(B1):771–786, 1993.
- 1298 [29] Judith S Chester and Raymond C Fletcher. Stress distribution and failure
1299 in anisotropic rock near a bend on a weak fault. *Journal of Geophysical*
1300 *Research: Solid Earth*, 102(B1):693–708, 1997.
- 1301 [30] Michele L Cooke. Fracture localization along faults with spatially varying
1302 friction. *Journal of Geophysical Research: Solid Earth*, 102(B10):22425–
1303 22434, 1997.
- 1304 [31] ML Cooke and DD Pollard. Bedding-plane slip in initial stages of fault-
1305 related folding. *Journal of Structural Geology*, 19(3-4):567–581, 1997.
- 1306 [32] Patience A Cowie and Zoe K Shipton. Fault tip displacement gradients and
1307 process zone dimensions. *Journal of Structural Geology*, 20(8):983–997, 1998.
- 1308 [33] Steven L Crouch and AM Starfield. *Boundary element methods in solid*
1309 *mechanics: with applications in rock mechanics and geological engineering*.
1310 Allen & Unwin, 1982.
- 1311 [34] NC Davatzes and A Aydin. Distribution and nature of fault architecture in
1312 a layered sandstone and shale sequence: An example from the moab fault,
1313 utah. 2005.

- 1314 [35] Nicholas C Davatzes, Atilla Aydin, and Peter Eichhubl. Overprinting fault-
1315 ing mechanisms during the development of multiple fault sets in sandstone,
1316 chimney rock fault array, utah, usa. *Tectonophysics*, 363(1):1–18, 2003.
- 1317 [36] Guy Davidesko, Amir Sagy, and Yossef H Hatzor. Evolution of slip surface
1318 roughness through shear. *Geophysical Research Letters*, 41(5):1492–1498,
1319 2014.
- 1320 [37] James H Dieterich and Deborah Elaine Smith. Nonplanar faults: Mechanics
1321 of slip and off-fault damage. In *Mechanics, Structure and Evolution of Fault*
1322 *Zones*, pages 1799–1815. Springer, 2009.
- 1323 [38] Eric M Dunham, David Belanger, Lin Cong, and Jeremy E Kozdon. Earth-
1324 quake ruptures with strongly rate-weakening friction and off-fault plasticity,
1325 part 2: Nonplanar faults. *Bulletin of the Seismological Society of America*,
1326 101(5):2308–2322, 2011.
- 1327 [39] James T Engelder. Cataclasis and the generation of fault gouge. *Geological*
1328 *Society of America Bulletin*, 85(10):1515–1522, 1974.
- 1329 [40] James P Evans. Thickness-displacement relationships for fault zones. *Jour-*
1330 *nal of structural geology*, 12(8):1061–1065, 1990.
- 1331 [41] Zijun Fang and Eric M Dunham. Additional shear resistance from fault
1332 roughness and stress levels on geometrically complex faults. *Journal of Geo-*
1333 *physical Research: Solid Earth*, 118(7):3642–3654, 2013.
- 1334 [42] Haakon Fossen and Jonny Hesthammer. Deformation bands and their sig-
1335 nificance in porous sandstone reservoirs. *First Break*, 16(1):21–25, 1998.

- 1336 [43] Haakon Fossen, Tord Erlend Skeie Johansen, Jonny Hesthammer, and
1337 Atle Rotevatn. Fault interaction in porous sandstone and implications
1338 for reservoir management; examples from southern utah. *AAPG bulletin*,
1339 89(12):1593–1606, 2005.
- 1340 [44] Haakon Fossen, Richard A Schultz, Zoe K Shipton, and Karen Mair. De-
1341 formation bands in sandstone: a review. *Journal of the Geological Society*,
1342 164(4):755–769, 2007.
- 1343 [45] JA Greenwood and JBP Williamson. Contact of nominally flat surfaces. In
1344 *Proceedings of the Royal Society of London A: Mathematical, Physical and*
1345 *Engineering Sciences*, volume 295, pages 300–319. The Royal Society, 1966.
- 1346 [46] W Ashley Griffith, Stefan Nielsen, Giulio Di Toro, and Steven AF Smith.
1347 Rough faults, distributed weakening, and off-fault deformation. *Journal of*
1348 *Geophysical Research: Solid Earth*, 115(B8), 2010.
- 1349 [47] Christopher Harbord, Stefan Nielsen, and Nicola De Paola. Fault zone rough-
1350 ness controls slip stability. In *EGU General Assembly Conference Abstracts*,
1351 volume 18, page 9799, 2016.
- 1352 [48] Rebecca M Harrington and Emily Brodsky. Smooth, mature faults radiate
1353 more energy than rough, immature faults in parkfield, ca. *Bulletin of the*
1354 *Seismological Society of America*, 99(4):2323–2334, 2009.
- 1355 [49] RR Jones, S Kokkalas, and KJW McCaffrey. Quantitative analysis and
1356 visualization of nonplanar fault surfaces using terrestrial laser scanning (li-
1357 dar)—the arkitsa fault, central greece, as a case study. *Geosphere*, 5(6):465–
1358 482, 2009.

- 1359 [50] Vincent Cooper Kelley and N James Clinton. *Fracture systems and tectonic*
1360 *elements of the Colorado Plateau*. Number 6-7. University of New Mexico
1361 Press, 1960.
- 1362 [51] Bill Kilsdonk and Raymond C Fletcher. An analytical model of hanging-wall
1363 and footwall deformation at ramps on normal and thrust faults. *Tectono-*
1364 *physics*, 163(1-2):153–168, 1989.
- 1365 [52] S Kokkalas, RR Jones, KJW McCaffrey, and P Clegg. Quantitative fault
1366 analysis at arkitsa, central greece, using terrestrial laser-scanning (lidar).
1367 *Bulletin of the Geological Society of Greece*, 37:1–14, 2007.
- 1368 [53] Robert W Krantz. Orthorhombic fault patterns: the odd axis model and
1369 slip vector orientations. *Tectonics*, 8(3):483–495, 1989.
- 1370 [54] RW Krantz. Orthorhombic fault patterns and three-dimensional strain anal-
1371 ysis, northern san rafael swell, utah. In *Geological Society of America Ab-*
1372 *stracts with Programs*, volume 18, page 125, 1986.
- 1373 [55] Thorne Lay, Hiroo Kanamori, and Larry Ruff. *The asperity model and the*
1374 *nature of large subduction zone earthquakes*. na, 1982.
- 1375 [56] Joong-Jeek Lee and Ronald L Bruhn. Structural anisotropy of normal fault
1376 surfaces. *Journal of Structural Geology*, 18(8):1043–1059, 1996.
- 1377 [57] Alan V Levy and Nancy Jee. Unlubricated sliding wear of ceramic materials.
1378 *Wear*, 121(3):363–380, 1988.

- 1379 [58] Laurent Maerten, David D Pollard, and Frantz Maerten. Digital mapping of
1380 three-dimensional structures of the chimney rock fault system, central utah.
1381 *Journal of Structural Geology*, 23(4):585–592, 2001.
- 1382 [59] Benoit B Mandelbrot. Self-affine fractals and fractal dimension. *Physica*
1383 *scripta*, 32(4):257, 1985.
- 1384 [60] Benoit B Mandelbrot, Dann E Passoja, and Alvin J Paullay. Fractal char-
1385 acter of fracture surfaces of metals. 1984.
- 1386 [61] Jessica A McBeck, Elizabeth H Madden, and Michele L Cooke. Growth by
1387 optimization of work (grow): A new modeling tool that predicts fault growth
1388 through work minimization. *Computers & Geosciences*, 88:142–151, 2016.
- 1389 [62] KR McClay and PG Ellis. Analogue models of extensional fault geometries.
1390 *Geological Society, London, Special Publications*, 28(1):109–125, 1987.
- 1391 [63] Brendan J Meade. Algorithms for the calculation of exact displacements,
1392 strains, and stresses for triangular dislocation elements in a uniform elastic
1393 half space. *Computers & geosciences*, 33(8):1064–1075, 2007.
- 1394 [64] HC Meng and KC Ludema. Wear models and predictive equations: their
1395 form and content. *Wear*, 181:443–457, 1995.
- 1396 [65] MS Moreno, J Bolte, J Klotz, and Dr Melnick. Impact of megathrust ge-
1397 ometry on inversion of coseismic slip from geodetic data: Application to the
1398 1960 chile earthquake. *Geophysical Research Letters*, 36(16), 2009.
- 1399 [66] Rodrick Dane Myers. *Structure and hydraulics of brittle faults in sandstone*.
1400 PhD thesis, Stanford University, 1999.

- 1401 [67] Yoshimitsu Okada. Internal deformation due to shear and tensile faults in
1402 a half-space. *Bulletin of the Seismological Society of America*, 82(2):1018–
1403 1040, 1992.
- 1404 [68] Paul G Okubo and James H Dieterich. Effects of physical fault properties on
1405 frictional instabilities produced on simulated faults. *Journal of Geophysical
1406 Research: Solid Earth*, 89(B7):5817–5827, 1984.
- 1407 [69] Kenshiro Otsuki, Nobuaki Monzawa, and Toshiro Nagase. Fluidization and
1408 melting of fault gouge during seismic slip: Identification in the nojima fault
1409 zone and implications for focal earthquake mechanisms. *Journal of Geophys-
1410 ical Research: Solid Earth*, 108(B4), 2003.
- 1411 [70] Andrew Clell Palmer and JR Rice. The growth of slip surfaces in the pro-
1412 gressive failure of over-consolidated clay. In *Proceedings of the Royal Society
1413 of London A: Mathematical, Physical and Engineering Sciences*, volume 332,
1414 pages 527–548. The Royal Society, 1973.
- 1415 [71] William L Power and Terry E Tullis. Euclidean and fractal models for the
1416 description of rock surface roughness. *Journal of Geophysical Research: Solid
1417 Earth*, 96(B1):415–424, 1991.
- 1418 [72] William L Power, Terry E Tullis, and John D Weeks. Roughness and
1419 wear during brittle faulting. *Journal of Geophysical Research: Solid Earth*,
1420 93(B12):15268–15278, 1988.
- 1421 [73] WL Power, TE Tullis, SR Brown, GN Boitnott, and CH Scholz. Roughness
1422 of natural fault surfaces. *Geophysical Research Letters*, 14(1):29–32, 1987.

- 1423 [74] CA Queener, TC Smith, and WL Mitchell. Transient wear of machine parts.
1424 *Wear*, 8(5):391–400, 1965.
- 1425 [75] François Renard, Christophe Voisin, David Marsan, and Jean Schmittbuhl.
1426 High resolution 3d laser scanner measurements of a strike-slip fault quan-
1427 tify its morphological anisotropy at all scales. *Geophysical Research Letters*,
1428 33(4), 2006.
- 1429 [76] Elizabeth Ritz, David D Pollard, and Michael Ferris. The influence of fault
1430 geometry on small strike-slip fault mechanics. *Journal of Structural Geology*,
1431 73:49–63, 2015.
- 1432 [77] Eugene C Robertson et al. Continuous formation of gouge and breccia dur-
1433 ing fault displacement. In *The 23rd US Symposium on Rock Mechanics*
1434 (*USRMS*). American Rock Mechanics Association, 1982.
- 1435 [78] Amir Sagy and Emily E Brodsky. Geometric and rheological asperities in an
1436 exposed fault zone. *Journal of Geophysical Research: Solid Earth*, 114(B2),
1437 2009.
- 1438 [79] Amir Sagy, Emily E Brodsky, and Gary J Axen. Evolution of fault-surface
1439 roughness with slip. *Geology*, 35(3):283–286, 2007.
- 1440 [80] Francois Saucier, Eugene Humphreys, and Ray Weldon. Stress near geo-
1441 metrically complex strike-slip faults: application to the san andreas fault
1442 at cajon pass, southern california. *Journal of Geophysical Research: Solid*
1443 *Earth*, 97(B4):5081–5094, 1992.

- 1444 [81] Heather M Savage and Michele L Cooke. Unlocking the effects of friction on
1445 fault damage zones. *Journal of Structural Geology*, 32(11):1732–1741, 2010.
- 1446 [82] Jean Schmittbuhl, Sylvie Gentier, and Stéphane Roux. Field measurements
1447 of the roughness of fault surfaces. *Geophysical Research Letters*, 20(8):639–
1448 641, 1993.
- 1449 [83] Jean Schmittbuhl, Francois Schmitt, and Christopher Scholz. Scaling in-
1450 variance of crack surfaces. *Journal of Geophysical Research: Solid Earth*,
1451 100(B4):5953–5973, 1995.
- 1452 [84] Jean Schmittbuhl, Jean-Pierre Vilotte, and Stéphane Roux. Reliability of
1453 self-affine measurements. *Physical Review E*, 51(1):131, 1995.
- 1454 [85] CH Scholz and JT Engelder. The role of asperity indentation and ploughing
1455 in rock friction—i: Asperity creep and stick-slip. In *International Journal of*
1456 *Rock Mechanics and Mining Sciences & Geomechanics Abstracts*, volume 13,
1457 pages 149–154. Elsevier, 1976.
- 1458 [86] Ch H Scholz and CA Aviles. The fractal geometry of faults and faulting.
1459 *Earthquake source mechanics*, pages 147–155, 1986.
- 1460 [87] Christopher H Scholz. Wear and gouge formation in brittle faulting. *Geology*,
1461 15(6):493–495, 1987.
- 1462 [88] Richard A Schultz and Haakon Fossen. Displacement-length scaling in three
1463 dimensions: the importance of aspect ratio and application to deformation
1464 bands. *Journal of Structural Geology*, 24(9):1389–1411, 2002.

- 1465 [89] Paul Segall and DD Pollard. Mechanics of discontinuous faults. *Journal of*
1466 *Geophysical Research: Solid Earth*, 85(B8):4337–4350, 1980.
- 1467 [90] Katherine AH Shervais and James D Kirkpatrick. Smoothing and re-
1468 roughening processes: The geometric evolution of a single fault zone. *Journal*
1469 *of Structural Geology*, 91:130–143, 2016.
- 1470 [91] Zheqiang Shi and Steven M Day. Rupture dynamics and ground motion from
1471 3-d rough-fault simulations. *Journal of Geophysical Research: Solid Earth*,
1472 118(3):1122–1141, 2013.
- 1473 [92] ZK Shipton and PA Cowie. Damage zone and slip-surface evolution over μm
1474 to km scales in high-porosity navajo sandstone, utah. *Journal of Structural*
1475 *Geology*, 23(12):1825–1844, 2001.
- 1476 [93] Zoe K Shipton and Patience A Cowie. A conceptual model for the origin of
1477 fault damage zone structures in high-porosity sandstone. *Journal of Struc-*
1478 *tural Geology*, 25(3):333–344, 2003.
- 1479 [94] Zoe K Shipton, James P Evans, Kim R Robeson, Craig B Forster, and
1480 Stephen Snelgrove. Structural heterogeneity and permeability in faulted
1481 eolian sandstone: Implications for subsurface modeling of faults. *AAPG*
1482 *bulletin*, 86(5):863–883, 2002.
- 1483 [95] Zoe K Shipton, Aisling M Soden, James D Kirkpatrick, Aileen M Bright,
1484 and Rebecca J Lunn. How thick is a fault? fault displacement-thickness
1485 scaling revisited. *Earthquakes: Radiated energy and the physics of faulting*,
1486 pages 193–198, 2006.

- 1487 [96] RH Sibson. Fault rocks and fault mechanisms. *Journal of the Geological*
1488 *Society*, 133(3):191–213, 1977.
- 1489 [97] Richard H Sibson. Crustal stress, faulting and fluid flow. *Geological Society,*
1490 *London, Special Publications*, 78(1):69–84, 1994.
- 1491 [98] Mark W Stirling, Steven G Wesnousky, and Kunihiko Shimazaki. Fault
1492 trace complexity, cumulative slip, and the shape of the magnitude-frequency
1493 distribution for strike-slip faults: a global survey. *Geophysical Journal In-*
1494 *ternational*, 124(3):833–868, 1996.
- 1495 [99] R Summers and J Byerlee. A note on the effect of fault gouge composition on
1496 the stability of frictional sliding. In *International Journal of Rock Mechanics*
1497 and *Mining Sciences & Geomechanics Abstracts*, volume 14, pages 155–160.
1498 Elsevier, 1977.
- 1499 [100] Mark T Swanson. Sidewall ripouts in strike-slip faults. *Journal of Structural*
1500 *Geology*, 11(8):933–948, 1989.
- 1501 [101] Anita Torabi and Haakon Fossen. Spatial variation of microstructure and
1502 petrophysical properties along deformation bands in reservoir sandstones.
1503 *AAPG bulletin*, 93(7):919–938, 2009.
- 1504 [102] Peter Vrolijk, Rod Myers, Michael L Sweet, Zoe K Shipton, Ben Dock-
1505 rill, James P Evans, Jason Heath, and Anthony P Williams. Anatomy of
1506 reservoir-scale normal faults in central utah: Stratigraphic controls and im-
1507 plications for fault zone evolution and fluid flow. *Field Guides*, 6:261–282,
1508 2005.

- 1509 [103] Weibin Wang and Christopher H Scholz. Wear processes during frictional
1510 sliding of rock: a theoretical and experimental study. *JOURNAL OF GEO-*
1511 *PHYSICAL RESEARCH-ALL SERIES-*, 99:6789–6789, 1994.
- 1512 [104] Naoto YOSHIOKA. Fracture energy and the variation of gouge and surface
1513 roughness during frictional sliding of rocks. *Journal of Physics of the Earth*,
1514 34(4):335–355, 1986.
- 1515 [105] O Zielke, M Galis, and PM Mai. Fault roughness and strength heterogene-
1516 ity control earthquake size and stress drop. *Geophysical Research Letters*,
1517 44(2):777–783, 2017.
- 1518 [106] Olaf Zielke and Paul Martin Mai. Sub-patch roughness in earthquake rupture
1519 investigations. *Geophysical Research Letters*, 2016.

1520 8 Appendix

1521 8.1 Surface Processing scripts

1522 Or possibly a link to a git repository...

1523 8.2 User manual for script

1524 This manual should serve as both a basic guide to the logic and usage of the *surface*
1525 *processing package*.

1526 The master function of the package is *surfaceprocessing*. This function effec-
1527 tively deal with the inputs and direct computations towards the necessary func-
1528 tions. Outputs of the function are a .mat workspace file for each input data file.

1529 The workspace includes a structure (called *parameters*) with the raw surface anal-
1530 ysis outputs, the point spacing, the decimation factor (if any), the file name and
1531 the date of the analysis. The workspace also includes the grid form of the origi-
1532 nal inputed surface (called *surface*), and the pre-processed copy that was used for
1533 the subsequent analysis (called *zGrid*). Inputs are always included in pairs. The
1534 former defines the type of input, the latter qualifies or quantifies the input. This
1535 structure allows for adaptability of the code to various needs. Options include the
1536 following:

1537 • *what to do?*: 'toDo', followed by the desired analyses on of: 'FFT', 'PLOMB',
1538 'parameters' or 'all' (default is 'all') - can be a cell array. This specifies what
1539 kind of spatial analysis will be done on the input surface data. The spatial
1540 analysis is calculated and averaged across every single profiles along the
1541 surface. The analyses are the following:

- 1542 – 'FFT', a power spectrum computed using a Fast Fourier Transform
1543 (FFT) algorithm;
- 1544 – 'PLOMB', a power spectrum computed using a least-squares Lomb-
1545 Scargle algorithm;
- 1546 – 'paramters', the calculation (as a function of scale) of the Root Mean
1547 Squared (RMS), skewness, kurtosis and asymmetry averaged across all
1548 segments of a given length on all profiles of the surface.

1549 'all' simply performs all the analyses outlined above.

- 1550 • *skip pre-processing?*: 'bypass', followed by 'zygo', 'pre-processing' or 'no' to
1551 be used input is already in aligned clean grid form - input files are then

1552 (default is 'no'). 'zygo' is specifically adapted to the proprietary data format
1553 of the white light in Wong. 'pre-processing' simply skips any pre-processing.
1554 This option requires a .mat structure with a field named 'grid' with the
1555 topography and a field name 'pointSpacing' specifying the point spacing (in
1556 meters). In either case the topography must be aligned such that the positive
1557 x direction is the parallel direction.

1558 • *for the parameter analysis, how many scales?* 'numberOfScales' followed
1559 by the desired number of analysed scales. This option is relevant to the
1560 parameters analysis. Note that this has a lot of effect on the amount of
1561 processing time (default is 10).

1562 • *decimation:* 'decimationFactor' followed by the desired decimation factor
1563 (default is 1). Decimation is a useful tool to reduce computation time. The
1564 surface grid is sub-sampled according to the decimation such that a decima-
1565 tion factor of k would imply that only every k th point on the every k th will
1566 be considered for hte subsequent analysis.

1567 • *Instrument specific analysis* 'instrument' followed by 'white light', 'laser
1568 scanner' or 'lidar' (default does not set any instrument specific adjustments).
1569 Some instrument specific pre-processing steps are taken. Please contact me
1570 if you intend to use this as they may be highly dependent on the specific
1571 instrument used.

1572 For instance, *surfaceprocessing('todo','FFT','bypass','zygo')* will only perform
1573 a power spectral density analysis and will skip preprocessing and assume that all
1574 input will be in the 'zygo' export .xyz format.

1575 When the command is executed, the user will be prompted to navigate to the
1576 directory where the input data is located. IMPORTANT: the directory must *only*
1577 contain files of one data format. There cannot be other files or sub-directories
1578 in the directory. The user will then be prompted to choose a destination for the
1579 output data. The requirements for the output location are less stringent. However,
1580 it is advisable to choose an empty directory such as to facilitate subsequent steps.

1581 The next step is to visualize the output of the analysis. This is done using the
1582 *unpack parameters* function. This function provides various visualization options
1583 for all files in the directory chosen by the user. The first input (the *desired plot*)
1584 can be one of the following:

1585 'FFT': plot all power spectra;

1586 'PLOMB': periodogram plot as determined by the Lomb-Scargle least squares
1587 analysis;

1588 'topostd': plot of the root mean squared (RMS) as a function of scale;

1589 'topoSkew': plot of skewness of height fields as a function of segment scale;

1590 'topoKurt': plot of the the kurtoisis of height fields as a function of segment
1591 scale;

1592 'PowerVsDisp': plot of power interpolated at a given scale as a function of
1593 displacement;

1594 'RMSVsDisp': model RMS at a given scale as a function of displacement

1595 'Grids': shows both the original and pre-processed grid for the specified file
1596 'fileName';

1597 'Best Fits': best logarithmic fits to power spectra obtained from the fast
1598 fourrier transform analysis.

1599 The functionality of the packages is broadly divided into three sections: 1)
1600 importing and preprocessing data, 2) performing various spatial statistics on the
1601 pre-processed data, and 3) unpacking the analysis output into figures.

1602 In order to run smoothly the all functions included in the package should be
1603 kept in the same directory or on an accessible path.

1604 For reference, here is a quick outline of what each function does:

1605 *affine fit*: (from mathworks) Computes the plane of best fit using least
1606 squares normal distance;

1607 *align grid*: finds the smoothest directions in a grid using FFT spectra and
1608 rotates and re-grids the input grid;

1609 *fault spectral density simple*: Calculates the average lomb-scargle spectral
1610 density every row of a N by M array;

1611 *FindErr loop anisotropy*

1612 *flatten XYZ*: removes planar trends from XYZ data by applying a rotations
1613 matrix according to the best fit plane (*affine fit*);

1614 *fractal model outlier*: Removes outlying segments according to a near-gaussian
1615 model for the distribution of RMS values at specified segment lengths (or
1616 scales);

1617 *frequency spectrum*: Calculates the average lomb-scargle spectral density of
1618 all continuous segments on every single row of a N by M array;

1619 *parse 'zygo' format*: extracts the both the point spacing and topographic grid
1620 from the exported zygo format. Can also remove planar trend from data
1621 (substracted from grid);

1622 *rotateZ*: applies rotation matrix on XYZ data

1623 *surface 'analysis'*: Aggregates the analysis functions and applies them to an
1624 input grid

1625 *surface 'cleaning'*: removes outliers associated with surface defects

1626 *surface 'parameters'*: calculates spatial statistics and parameters along seg-
1627 ments as a function of scale (RMS, skewness, directional asymmetry and
1628 kurtosis)

1629 *surface 'preprocessing' 2*: deals with preprocessing input data (import data,
1630 cleaning and gridding data)

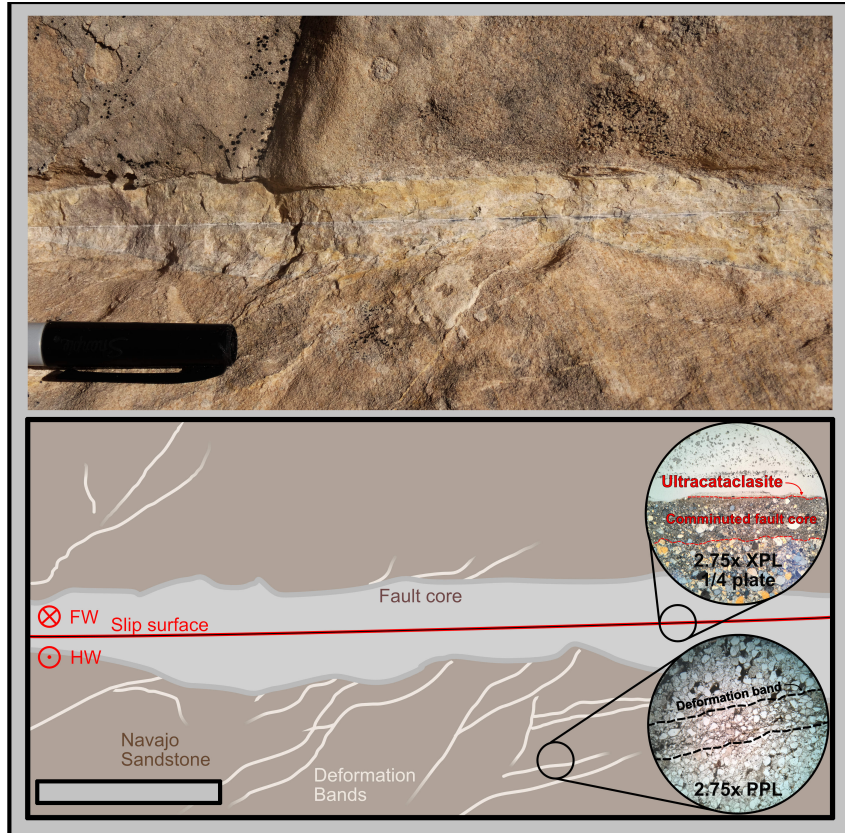


Figure 4: Top: Example of representative meso-structure of faults in the Navajo sandstone. Bottom: Cartoon of the representative meso-structure with slip surface (red), fault core (grey), deformation bands (pale beige) and intact host sand stone (brown). Upper half is the footwall; lower half is the hanging wall. Exposure is slip perpendicular. Representative thin sections show (not in situ) show the bottom half of the fault core (top) and deformation band (bottom). The section through the slip surface shows the microstructural architecture of slip surfaces with a very fine layer (barely visible) of ultracataclasite and a bounding comminuted layer. Note that this section is still well within the fault core. The section through the deformation bands shows the gradational reduction in grain size (outlined by black dashed line).

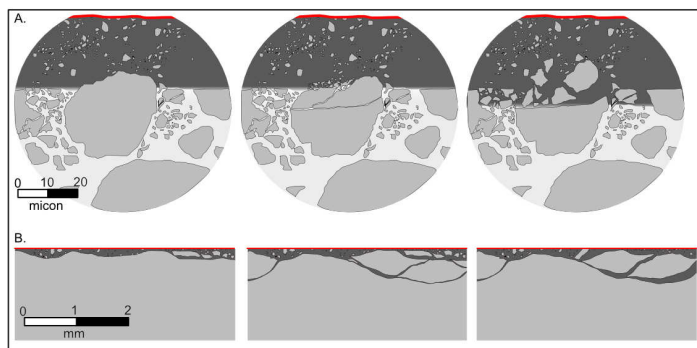


Figure 5: Schematic example of the interface between the cataclastic host and the fluidized ultracataclasite layer at two distinct length scales. A. at the length scale of ten's of microns grains, the shape of the interface is



Figure 6: Example of a slip surface interpreted as a principle slip surface with around 20 meters of displacement at Big Hole Fault



Figure 7: Left: Example of at least two distinct polished slip surfaces on the same fault structure. Right: Example of concentric pattern on cross-sectional view a fault

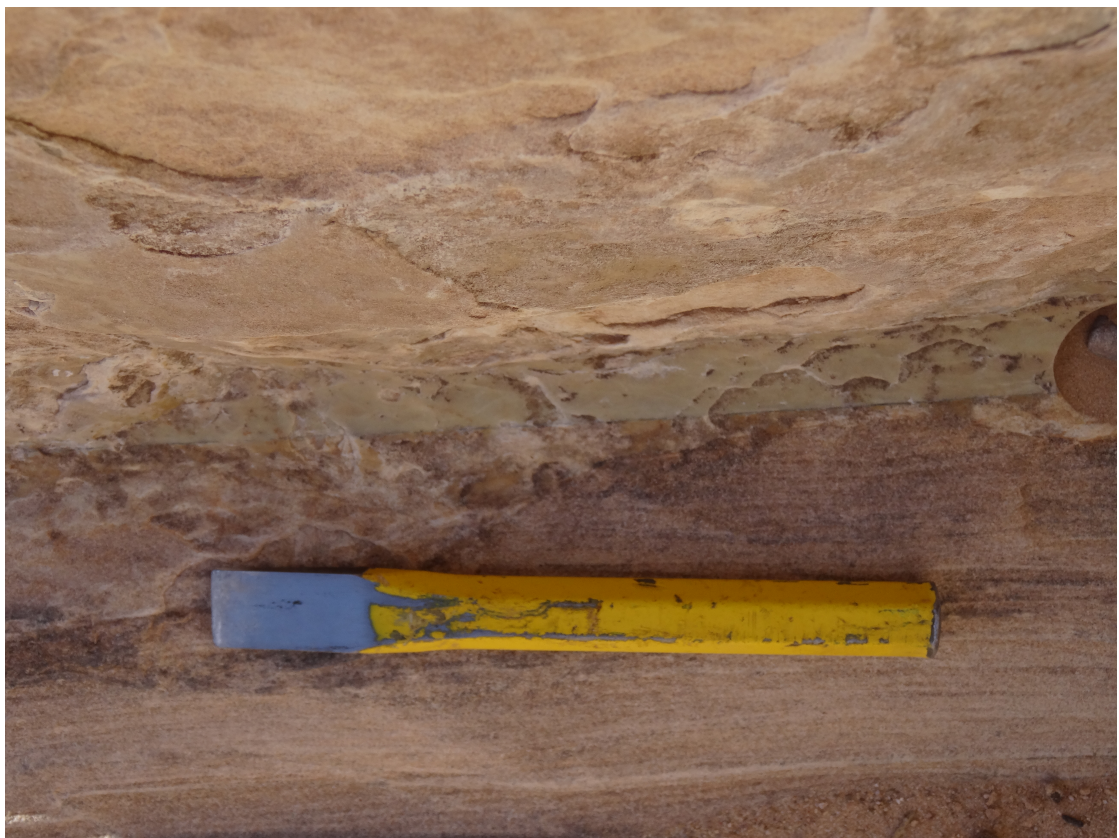


Figure 8: Example of a slip surface interpreted as a principle slip surface with around 20 meters of displacement at Big Hole Fault

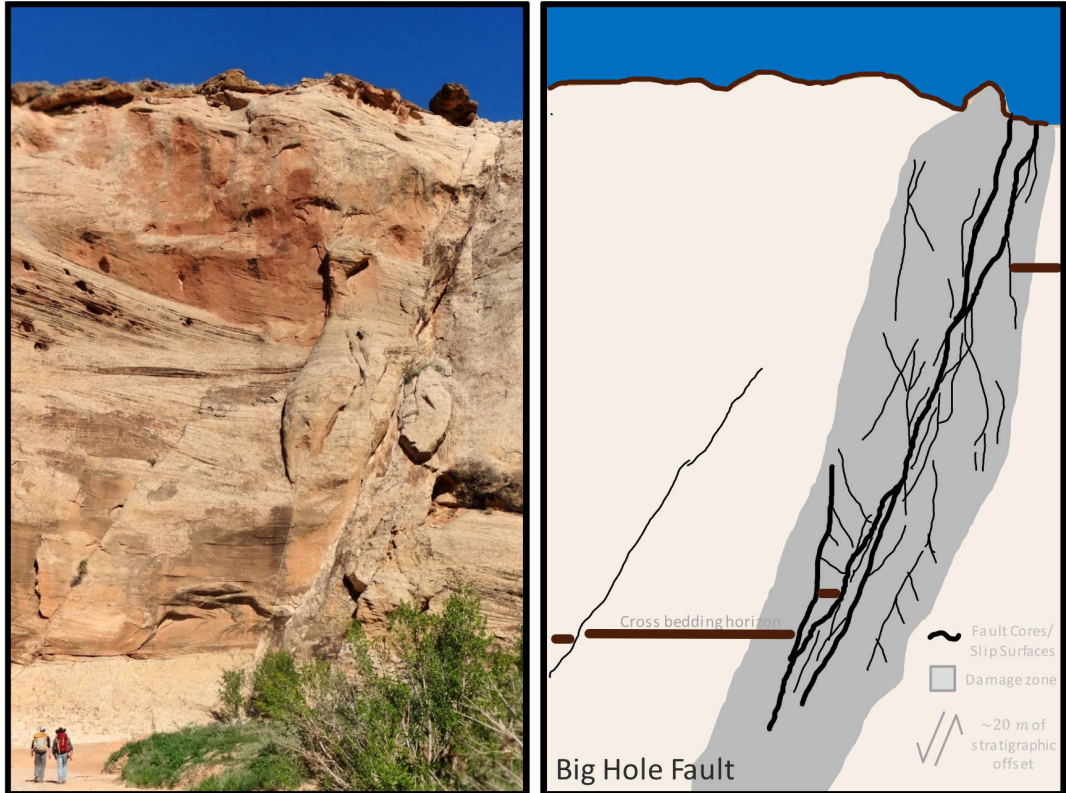


Figure 9: At Big Hole fault, two large-scale continuous strands of the fault, both accommodating meters of displacement exemplify problem at a larger scale. Due to the ambiguity, Shipton and Cowie, 2003 report large uncertainty on the partitioning of stratigraphic offset across the two strand

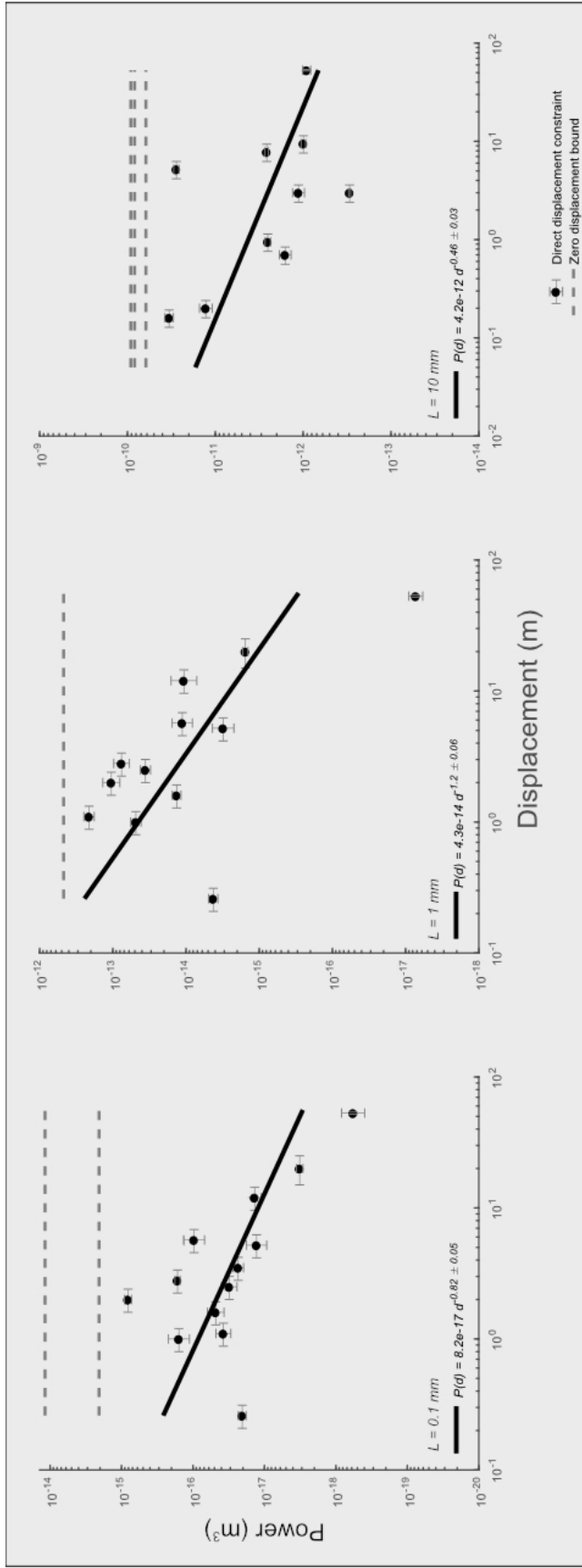


Figure 10: Roughness as a function of displacement at various scales (100 μm , 1 mm , and 1 cm). Best fit line indicated in black. Roughness of joints and/or deformation bands indicated with grey dashed line.

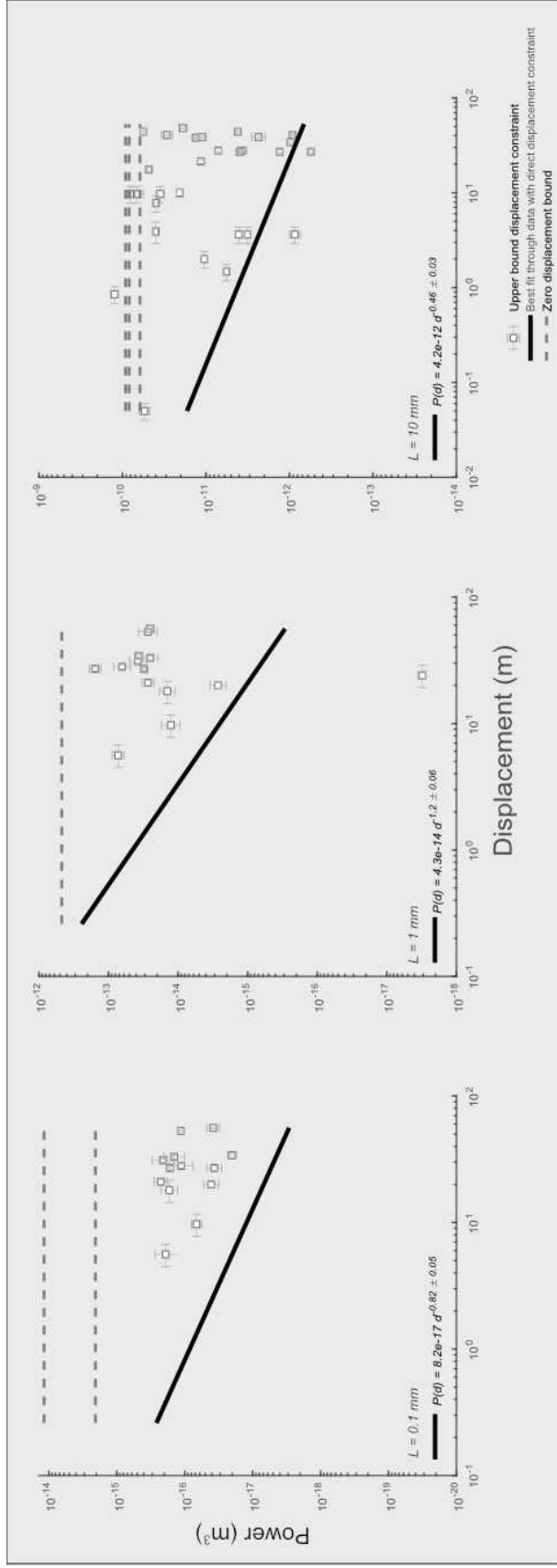


Figure 11: Roughness of faults with only maximum constraints on displacement as a function of displacement at various scales ($100 \mu\text{m}$, 1 mm , and 1 cm) compared to best fit through data with direct constraints on displacement. Best fit line indicated in black. Roughness of joints and/or deformation bands indicated with grey dashed line. Note that with the exception of a few outliers, the points with x -axes defined by maximum allowable displacement all obey the inequality physically required by the smoothing model best fit.